Diplomarbeit

Spontaneous decay in the multi-mode regime of cavity quantum electrodynamics

ausgeführt am

Institut für Theoretische Physik
der Technischen Universität Wien

Electrical Engineering Department
Princeton University

unter der Anleitung von

Prof. Stefan Rotter
Dipl.-Ing. Matthias Liertzer

Prof. Hakan E. Türeci

durch

Rafael Luger
Anton-Geiger-Weg 43
A-1160 Wien
rafael.luger@gmail.com

_____   _____
Datum   Unterschrift

Contents

Chapter 1.

Introduction

The process of spontaneous emission in an optical cavity is a fundamental problem in the field of quantum optics. The interest in this setup was sparked when E. Purcell first found that the emission rate of an atom in a cavity can be enhanced when its transition frequency is tuned to a cavity resonance [1].

Spontaneous emission can be explained within quantum electrodynamics (QED). An emitter couples to the vacuum fluctuations of the electromagnetic field, which eventually causes any excitations in the emitter to decay to the ground state. If the emitter is placed in an optical cavity the mode structure of the electromagnetic field is different from the vacuum, leading to a change in this decay and the corresponding emission characteristics. The study engaging the interaction of matter with light in confined cavities is called cavity quantum electrodynamics (CQED) [2, 3]. A popular model in CQED is the Jaynes-Cummings model (JCM). It treats the behavior of an emitter, approximated by a two-level system (TLS), coupling to a single mode of the electromagnetic field (single-mode coupling). Despite being limited to the interaction with just one mode of the electromagnetic field the JCM can explain many well known phenomena in quantum optics, like Rabi oscillations, and other coherent effects [4].

More than 65 years after Purcell's preceding work the seemingly simple system of an excited emitter in an optical cavity (see Fig. 1.1) is still the topic of current research. This is mostly due to a number of recent experimental implementations of this problem, for example Rydberg atoms coupling with a resonant mode [5, 6], quantum dots in the solid state [7] and even Qubits in superconducting resonators [8].

In this thesis we aim to go beyond the simple JCM to describe the coupling of an emitter to multiple cavity modes. For this purpose we employ a fully quantum approach [9], which was already successfully used to analytically solve suitably engineered cavities [10]. The local density of states (LDOS) [11] of these cavities was, however, such that an effective single-mode coupling approximation could be employed [12–14]. In the present work we go beyond this limitations and study systems in very different coupling regimes. In particular we are interested in the question, how an emitter decays when it couples to a large number of cavity modes
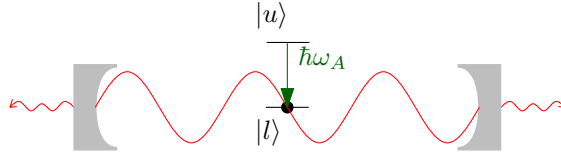
Figure 1.1.: A two-level system (TLS) emits a photon in an optical cavity. The emission characteristics of the TLS depend on the geometry of the cavity and the coupling strength of the TLS with the field modes.

which allow an emitted light pulse to return to the emitter after a finite amount of time.

We investigated one-dimensional systems, for coupling strengths covering 3 orders of magnitude. The influence of the geometry is taken into account through the cavity Green's function. For its calculation we make use of a recent development in laser theory, the so-called Constant-Flux (CF) states [15]. Such a biorthogonal set of basis functions proved to be very useful in laser theory to describe the constant photon flux outside the amplifying part of the laser. As we demonstrate in detail these boundary conditions also suit the problem of an excited emitter in a cavity. Hence applying this framework turns out very valuable for the numerical implementation and interpretation of the calculations performed in this thesis.

Our numerical scheme is completely general and can treat spontaneous decay in cavities with an arbitrary distribution of the index of refraction. First results are obtained for two different cavities in the single-mode, few-mode and multi-mode coupling regime are presented. We investigate a simple dielectric slab with and without $\lambda/4$-layers on both ends. We identify a new and interesting regime where the decay of the emitter through multiple modes leads to a quasi-classical sequence of reabsorption events in which the emitter gets re-excited by the return of the emitted wave packet. This results opens up many interesting, possibilities both for further theoretical and experimental studies alike.

Chapter 2.

Dynamics of an excited two-level system

In this chapter we derive the basic equations to describe the interaction of an emitter with its surrounding medium. We use a purely quantum mechanical approach [10] to the problem. In this method the emitter is represented by a two-level system (TLS) which is placed in an environment with a complex refractive index with an arbitrary space and frequency dependence.

2.1. Maxwell Equations

Our starting relations [9] are the classical Maxwell equations

$$\nabla \cdot \mathbf{B}(\mathbf{r}, t) = 0, \tag{2.1}$$

$$\nabla \cdot \mathbf{D}(\mathbf{r}, t) = \rho(\mathbf{r}, t), \tag{2.2}$$

$$\nabla \times \mathbf{E}(\mathbf{r}, t) + \frac{\partial}{\partial t} \mathbf{B}(\mathbf{r}, t) = 0, \tag{2.3}$$

$$\nabla \times \mathbf{H}(\mathbf{r}, t) - \frac{\partial}{\partial t} \mathbf{D}(\mathbf{r}, t) = \mathbf{j}(\mathbf{r}, t). \tag{2.4}$$

Without magnetization, we have $\mathbf{D}(\mathbf{r}, t) = \epsilon_0 \mathbf{E}(\mathbf{r}, t) + \mathbf{P}$, $\mathbf{B}(\mathbf{r}, t) = \mu_0 \mathbf{H}(\mathbf{r}, t)$, $\mathbf{j}(\mathbf{r}, t) = \sigma \mathbf{E}(\mathbf{r}, t)$. Applying the rotor on both sides of (2.3) gives

$$\nabla \times \nabla \times \mathbf{E}(\mathbf{r}, t) + \partial_t \left(\partial_t \epsilon_0 \mathbf{E}(\mathbf{r}, t) + \partial_t \mathbf{P}(\mathbf{r}, t) + \sigma \mathbf{E}(\mathbf{r}, t) \right) = 0. \tag{2.5}$$

Taking the Fourier transform[1] of (2.5) we get

$$\nabla \times \nabla \times \mathbf{E}(\mathbf{r}, \omega) + \frac{\omega^2}{c^2} \mathbf{E}(\mathbf{r}, \omega) + \mu_0 \sigma \omega \mathbf{E}(\mathbf{r}, \omega) = -\mu_0 \omega^2 \mathbf{P}(\mathbf{r}, \omega). \tag{2.6}$$

---

[1] We use the following convention for the Fourier transform:

$$X(\mathbf{r}, t) = \int_{-\infty}^{\infty} X(\mathbf{r}, \omega) e^{-i\omega t} \, \mathrm{d}\omega$$

$$X(\mathbf{r}, \omega) = \frac{1}{2\pi} \int_{-\infty}^{\infty} X(\mathbf{r}, t) e^{i\omega t} \, \mathrm{d}t$$

Functions, Operators etc. and their Fourier transform are distinguished by their respective dependencies (that is t and ω)

The polarization can be split up into two parts $\mathbf{P}(\mathbf{r}, \omega) = \mathbf{P}_L(\mathbf{r}, \omega) + \mathbf{P}_S(\mathbf{r}, \omega)$. $\mathbf{P}_S(\mathbf{r}, \omega)$ describes the nonlinear response of the source itself, taking photon emission and absorption of the source into account. $\mathbf{P}_L(\mathbf{r}, \omega)$ describes the linear response of the medium the source is placed in. This linear response can simply be treated using the well known relation $\mathbf{P}(\mathbf{r}, \omega) = \epsilon_0 \chi_e(\omega) \mathbf{E}(\mathbf{r}, \omega)$ and $n(\omega)^2 = \epsilon(\omega) = \epsilon_0(1 + \chi_e(\omega))$. We also assume to have no free charges ($\rho(\mathbf{r}, t) = 0$) therefore $\nabla \cdot \mathbf{E}(\mathbf{r}, \omega) = 0$. Setting also the conductivity $\sigma = 0$, we have

$$\left(\Delta + n(\omega)^2 \frac{\omega^2}{c^2} \right) \mathbf{E}(\mathbf{r}, \omega) = -\frac{1}{\epsilon_0} \frac{\omega^2}{c^2} \mathbf{P}_S(\mathbf{r}, \omega). \tag{2.7}$$

This equation can be solved using the Green's function formalism

$$\left(\Delta + n(\omega)^2 \frac{\omega^2}{c^2} \right) \mathbf{G}(\mathbf{r}, \mathbf{r}', \omega) = -\boldsymbol{\delta}(\mathbf{r} - \mathbf{r}'), \tag{2.8}$$

$$\mathbf{E}(\mathbf{r}, \omega) = \frac{1}{\epsilon_0} \frac{\omega^2}{c^2} \int \mathrm{d}^3 r' \, \mathbf{G}(\mathbf{r}, \mathbf{r}', \omega) \cdot \mathbf{P}_S(\mathbf{r}', \omega). \tag{2.9}$$

Equation (2.9) is a classical description of the electric field. In the next section we will demonstrate how the quantum nature of the electric field can be taken into account.

2.2. Introducing Bosonic fields

For this purpose we introduce a continuum set of bosonic fields [10] $\hat{\mathbf{f}}^\dagger$ and $\hat{\mathbf{f}}$, satisfying the relations

$$\left[\hat{f}_i(\mathbf{r}, \omega), \hat{f}_j^\dagger(\mathbf{r}', \omega') \right] = \delta_{ij} \delta(\mathbf{r} - \mathbf{r}') \delta(\omega - \omega'), \tag{2.10}$$

$$\left[\hat{f}_i(\mathbf{r}, \omega), \hat{f}_j(\mathbf{r}', \omega') \right] = \left[\hat{f}_i^\dagger(\mathbf{r}, \omega), \hat{f}_j^\dagger(\mathbf{r}', \omega') \right] = 0. \tag{2.11}$$

These operators describe the creation and annihilation of a photon of frequency ω at position $\mathbf{r}$. They can be used to describe the polarization caused by the emitter quantum mechanically

$$\hat{\mathbf{P}}_S(\mathbf{r}, \omega) = i \sqrt{\frac{\hbar \epsilon_0}{\pi} \mathrm{Im}\, \epsilon(\mathbf{r}, \omega)} \, \hat{\mathbf{f}}(\mathbf{r}, \omega). \tag{2.12}$$

Simply plugging this relation into Eq. (2.9) yields an expression for the electric field operator

$$\hat{\mathbf{E}}(\mathbf{r}, \omega) = i \sqrt{\frac{\hbar}{\pi \epsilon_0}} \frac{\omega^2}{c^2} \int \mathrm{d}^3 r' \, \sqrt{\mathrm{Im}\, \epsilon(\mathbf{r}', \omega)} \mathbf{G}(\mathbf{r}, \mathbf{r}', \omega) \cdot \hat{\mathbf{f}}(\mathbf{r}', \omega). \tag{2.13}$$

2.3. Hamiltonian

In the case considered here the emitter is an atom placed in a medium. Its Hamiltonian can be split into three parts, describing the field, the kinetic energy and the Coulomb energy.

$$\hat{H} = \hat{H}_{\text{field}} + \hat{H}_{\text{kin}} + \hat{H}_{\text{Coulomb}}. \tag{2.14}$$

The field energy, Eq. (2.15), can be described by the bosonic field operators introduced in the last section

$$\hat{H}_{\text{field}} = \int \mathrm{d}^3\mathbf{r} \int_0^\infty \mathrm{d}\omega \, \hbar\omega \, \hat{\mathbf{f}}^\dagger(\mathbf{r}, \omega) \cdot \hat{\mathbf{f}}(\mathbf{r}, \omega). \tag{2.15}$$

For the kinetic energy the minimal coupling scheme can be applied

$$\hat{H}_{\text{kin}} = \sum_\alpha \frac{1}{2m_\alpha} \left[\hat{\mathbf{p}}_\alpha - q_\alpha \hat{\mathbf{A}}(\hat{\mathbf{r}}_\alpha) \right] \cdot \left[\hat{\mathbf{p}}_\alpha - q_\alpha \hat{\mathbf{A}}(\hat{\mathbf{r}}_\alpha) \right]. \tag{2.16}$$

For the Coulomb energy two terms arise

$$\hat{H}_{\text{Coulomb}} = \frac{1}{2} \int \mathrm{d}^3\mathbf{r} \hat{\rho}_A(\mathbf{r}) \hat{\phi}_A(\mathbf{r}) + \int \mathrm{d}^3\mathbf{r} \hat{\rho}_A(\mathbf{r}) \hat{\phi}(\mathbf{r}). \tag{2.17}$$

The first one describes the energy between the particles and the second one the energy of the particles in the medium, where

$$\hat{\phi}_A(\mathbf{r}) = \int \mathrm{d}\mathbf{r}' \frac{\hat{\rho}_A(\mathbf{r}')}{4\pi\epsilon_0 |\mathbf{r} - \mathbf{r}'|} \quad \text{and} \quad \hat{\rho}_A(\mathbf{r}) = \sum_\alpha q_\alpha \delta(\mathbf{r} - \hat{\mathbf{r}}_\alpha). \tag{2.18}$$

Applying the electric dipole approximation and the rotating wave approximation yields the following Hamiltonian (for a detailed derivation we refer to [10] and to appendix A)

$$\hat{H} = \underbrace{\int \mathrm{d}^3\mathbf{r} \int_0^\infty \mathrm{d}\omega \, \hbar\omega \, \hat{\mathbf{f}}^\dagger(\mathbf{r}, \omega) \cdot \hat{\mathbf{f}}(\mathbf{r}, \omega)}_{\hat{H}_{\text{field}}} + \underbrace{\frac{1}{2}\hbar\omega_A \hat{\sigma}_z}_{\hat{H}_{\text{Atom}}} - \underbrace{[\hat{\sigma}_+ \hat{\mathbf{E}}^{(+)}(\mathbf{r}_A) \cdot \boldsymbol{\mu} + \text{H.c.}]}_{\hat{H}_{\text{Atom-field}}}.$$
$$\tag{2.19}$$

Note that we have replaced here the atom by a two-level system (TLS). The TLS consists only of a ground state and an excited state separated by the excitation energy $\hbar\omega_A$. This Hamiltonian provides the necessary basis to describe the interaction of the TLS with its surroundings.

2.4. Dynamics

We are interested in the time-dependence of the upper state occupation probability $|C_u|^2$ of the TLS given here in terms of the time-dependent amplitude $C_u(t)$. For this purpose we make the following ansatz for the wave-function

$$|\psi\rangle = C_u(t)e^{-i\omega_A t/2}|u\rangle|0\rangle + \int \mathrm{d}^3\mathbf{r} \int_0^\infty \mathrm{d}\omega\, C_{li}(\mathbf{r},\omega,t)e^{-i(\omega-\omega_A/2)t}|l\rangle|1_i(\mathbf{r},\omega)\rangle, \tag{2.20}$$

where $|l\rangle$ and $|u\rangle$ describe the lower state and upper state of the TLS. The states of the electric field are denoted by $|0\rangle$ for the vacuum state and $|1_i(\mathbf{r},\omega)\rangle$ for a single photon with the frequency ω at the position $\mathbf{r}$. Note that we have neglected here the vector character of the electric field, of the dipole operator and of the bosonic fields such that the Green's function becomes a scalar function instead of a tensor. In a next step we insert Eq. (2.20) into the Schrödinger equation using the Hamiltonian Eq. (2.19) and the electric field Eq. (2.13) derived in the last section. After some additional algebra (presented in detail in appendix B), we arrive at an integro-differential equation for the complex amplitude $C_u(t)$

$$\dot{C}_u(t) = \int_0^t \mathrm{d}t'\, K(t-t')C_u(t'), \tag{2.21}$$

containing the kernel function,

$$K(t-t') = -\frac{\mu^2}{\hbar\pi\epsilon_0} \int_0^\infty \mathrm{d}\omega \frac{\omega^2}{c^2} e^{-i(\omega-\omega_A)(t-t')} \mathrm{Im}\, G(\mathbf{r}_A,\mathbf{r}_A,\omega). \tag{2.22}$$

The frequency integral in the kernel Eq. (2.22) contains the imaginary part of the Green's function evaluated at the position of the emitter $\mathbf{r}_A$. The equation for C_u can be simplified by taking the time integration on both sides of Eq. (2.21). To do so an initial value for C_u is necessary at time $t = 0$. Since we are interested in the decay of the TLS, we choose the system to be in the excited state at the time $t = 0$, corresponding to $C_u(0) = 1$. With this we arrive at a Volterra integral equation of the second kind for the upper state occupation amplitude,

$$C_u(t) = \int_0^t \mathrm{d}t'\, \overline{K}(t-t')C_u(t') + 1, \tag{2.23}$$

and a corresponding kernel function,

$$\overline{K}(t-t') = \frac{\mu^2}{\hbar\pi\epsilon_0} \int_0^\infty \mathrm{d}\omega \frac{\omega^2}{c^2} \left(\frac{e^{-i(\omega-\omega_A)(t-t')} - 1}{i(\omega-\omega_A)} \right) \mathrm{Im}\, G(\mathbf{r_A},\mathbf{r_A},\omega). \tag{2.24}$$

The above two Eqs. (2.23) and (2.24) will be the basis for our investigations throughout this thesis. Solving these equations is, however, non-trivial and requires numerical techniques that we will present below. Analytical solutions can be found only in exceptional cases, as when the so-called Markov-approximation is applied.

2.5. The Markov Approximation

In the Markov approximation it is assumed that the surroundings of the emitter are not influenced by it, such that all memory effects of the system are disregarded. Obviously this is a very good approximation for big cavities, small refractive index variations and, most of all, for the vacuum. We start from Eq. (2.21) where the kernel is only different from zero within the correlation time τ_c [9]. In the Markov approximation τ_c is assumed to be very small compared to the time scale of any changes in the system. Hence $C_u(t')$ can be replaced by $C_u(t)$ and the upper integration limit t can be extended to infinity (as long as $t > \tau_c$) with very little error. We obtain a differential equation for C_u

$$\dot{C}_u(t) = C_u(t) \underbrace{\int_0^\infty K(t - t') \, \mathrm{d}t'}_{=\overline{K}_M(t-t')} . \tag{2.25}$$

In this way we impose that the value of C_u at time t does not depend on earlier times $t' < t$. We then have [10]

$$\overline{K}_M(t - t') = -\frac{\mu^2}{\hbar\pi\epsilon_0} \int_0^\infty \mathrm{d}\omega \, \frac{\omega^2}{c^2} \mathrm{Im}\, G(\mathbf{r}_A, \mathbf{r}_A, \omega) \int_0^\infty \mathrm{d}t' \, e^{-i(\omega - \omega_A)(t-t')}. \tag{2.26}$$

The time-integral can be solved using the distribution

$$\int_0^\infty \mathrm{d}\tau e^{-i\omega\tau} = \pi\delta(\omega) - \mathcal{P}\left(\frac{1}{\omega}\right). \tag{2.27}$$

The left over frequency integral is time independent, so the kernel becomes a constant with respect to time in the Markov approximation

$$\overline{K}_M(t - t') = -\frac{1}{2}\Gamma + i\delta\omega, \tag{2.28}$$

where we used the definitions for the line shift,

$$\delta\omega = \frac{k_A^2 \mu^2}{\pi\hbar\epsilon_0} \mathcal{P} \int_0^\infty \mathrm{d}\omega \, \frac{\mathrm{Im}\, G(\mathbf{r}_A, \mathbf{r}_A, \omega)}{(\omega - \omega_A)}, \tag{2.29}$$

and the (Markov) decay rate,

$$\Gamma = \frac{2k_A^2 \mu^2}{\hbar\epsilon_0} \mathrm{Im}\, G(\mathbf{r}_A, \mathbf{r}_A, \omega_A). \tag{2.30}$$

With these approximations it becomes very easy to solve the differential equation for C_u. The upper state occupation amplitude is then described simply by an exponential decay

$$C_u(t) = \exp(-\frac{1}{2}\Gamma + i\delta\omega). \tag{2.31}$$

In the Markov approximation it is easy to see that the line shift does not contribute to the occupation probability $|C_u(t)|^2$. In a slightly different approach [9] the line shift, Eq. (2.29), is included in the TLS transition frequency $\tilde{\omega}_A = \omega_A + \delta\omega$ and a shifted upper state amplitude $\tilde{C}_u(t) = C_u(t)e^{i\delta\omega t}$ is calculated. Hence the line shift is nothing but a frequency shift of the upper state amplitude. In many cases the line shift does not converge. This is a well known problem in the field of QED and referred to as Lamb shift. We will further discuss the problem of diverging solutions in section 3.2.

As mentioned already the Markov approximation works primely in free space. It also works very well in cavities during times smaller than the return time. The return time is given as $t_r = 2\,n\,c\,d$, where d is the distance from the emitter to the closest variation in the refractive index. It is the earliest time at which the TLS receives information about the dimensions of the cavity. We will further discuss its importance in section 3.2.1 and chapter 4.

These considerations already demonstrate the limited applicability of analytical techniques for general problems. In fact, for most real-world scenarios neither the Markov approximation, nor other approximations allowing for analytical solution, are applicable. Even in the most simple case of a dielectric slab (section 4.1) a complex interaction of the emitter with the electromagnetic field is observed. This can be described by the numerical techniques to be introduced below.

Chapter 3.

Numerical Solution Strategies

In the last chapter we derived Eqs. (2.23) and (2.24) to describe the dynamics of a two-level system (TLS). Our goal is to implement a numerical framework capable of calculating the emission characteristics of a TLS in one-dimensional cavities. We limit our approach to one dimension, not only due to the computational effort required in two- and three-dimensional systems. Our interest is in observing the emission characteristics of a TLS depending on the coupling with the field. This dependence can already be studied satisfactorily using one-dimensional cavities. Furthermore there are also experimental realizations of this problem [8]. In this chapter we discuss the boundary conditions used to calculate the Green's function and the adaptations of the kernel integral Eq. (2.24) to facilitate a numerical solution. In the last section of this chapter we present the numerical techniques used to obtain the results discussed in the next chapter.

3.1. Constant-Flux States

One of the most important ingredients to investigate the behavior of an emitter in an optical cavity is the Green's function, as it contains all the information about the electromagnetic field modes that enter into the calculation. Numerically the best way to calculate it, is to solve to Helmholtz-equation (2.8) directly. This brings up the question regarding the proper boundary conditions. As mentioned already we are interested in a general numerical solution for arbitrary one-dimensional cavities. Independent of their individual design, they all have in common that they are of finite size. Outside of the cavity the refractive index remains constant and therefore there will be no reflection into the cavity from outside. Also we constrain the refractive index outside of the cavity to real values (no absorption and no gain).

To treat environments of this kind we use the so-called Constant-Flux (CF) states. They form a complete, biorthogonal basis and allow for a spectral representation of the Green's function. They were originally designed to describe open laser systems, but also prove useful for the systems studied here. We give a brief introduction to CF states, since they are not only very useful numerical tools, but they also play

an important role in determining how well bound certain modes in a cavity are (see [15, 16] for a comprehensive review).

As their name already suggests CF states conserve the photon flux outside of the cavity. Inside the cavity they have complex eigenvalues, which are functions of the wavenumber k, i.e. the wavenumber of the electromagnetic field outside of the cavity. Their defining equations are

$$\left(\Delta + n^2(x, k)k_m^2(k)\right)\varphi_m(x, k) = 0 \qquad \text{for } \forall x \in \mathcal{C}, \qquad (3.1)$$

$$\left(\Delta + n^2(x, k)k^2\right)\varphi_m(x, k) = 0 \qquad \text{for } \forall x \notin \mathcal{C}, \qquad (3.2)$$

where $\mathcal{C}$ denotes the cavity. The media we are considering never have gain or loss, hence the refractive index $n(x, k)$ is real and the imaginary part of the k_m is always negative [17]. The main motivation for us to calculate the CF states was to observe the imaginary part of the CF eigenvalues, which measures how well the corresponding state is bound in the cavity. The smaller the absolute value of the imaginary part of k_m is, the longer the photon will stay in the cavity. In the limit of a closed system the eigenvalues are real and there is no loss. For the numerical treatment of higher dimensional systems it is important to apply the boundary conditions in such a way, thatso there is no backscattering into the cavity $\mathcal{C}$ (this is not an issue in one dimension). Therefore the general CF boundary conditions [15, 16] simplify in one dimensional systems to

$$\frac{\partial}{\partial x}\varphi_m(x, k) = ik\varphi_m(x, k) \qquad \text{for } \forall x \notin \mathcal{C}. \qquad (3.3)$$

Due to the imaginary unit in Eq. (3.3) the CF boundary conditions are in general not Hermitian. As a consequence, the CF states φ_m are not orthogonal to each other, but there exists a bi-orthogonal set $\overline{\varphi}_m$ that is defined by

$$\left(\Delta + n^2(x, k)\overline{k}_m^2(k)\right)\overline{\varphi}_m(x, k) = 0 \qquad \text{for } \forall x \in \mathcal{C}, \qquad (3.4)$$

$$\left(\Delta + n^2(x, k)k^2\right)\overline{\varphi}_m(x, k) = 0 \qquad \text{for } \forall x \notin \mathcal{C}, \qquad (3.5)$$

which fulfills a bi-orthogonality relation with the set φ_m

$$\langle\overline{\varphi}_m|\varphi_n\rangle = \int_{\mathcal{C}} n^2(x, k)\overline{\varphi}_m^*(x, k)\varphi_n(x, k)\,\mathrm{d}x = \eta_n\delta_{nm}, \qquad (3.6)$$

where η_n is a normalization constant. Using the relations above and Eq. (2.8) the Green's function can be expressed through a spectral expansion of the CF states

$$G(x, x', k) = \sum_m \frac{\overline{\varphi}_m^*(x', k)\varphi(x, k)}{(k^2 - k_m^2)} \qquad \text{for } \forall\, x, x' \in \mathcal{C}. \qquad (3.7)$$

3.2. Dealing with divergent solutions

One encounters a major obstacle when trying to calculate $C_u(t)$ following the kernel integral Eq. (2.24), as the integral does not converge. In this chapter we will discuss the necessary steps to get a meaningful numerical solution of the kernel integral.

3.2.1. Separating the Green's function

As the upper limit of the integration in Eq. (2.24) is not finite, it turns out to be difficult to solve the integral numerically. Cutting off the integration limit is thus required. The integral is performed over the Green's function and a weighting factor of the following form (we will only look at the real part, for reasons which will become clear later)

$$\frac{\sin\left((\omega - \omega_A)\tau\right)}{\omega - \omega_A}. \tag{3.8}$$

As shown in Fig. 3.1 the first and most dominant peak of this function becomes wider for smaller times τ. The smaller τ is the more frequencies are thus contributing, which makes it harder to get a numerically stable value for $\overline{K}(\tau)$. For infinitely

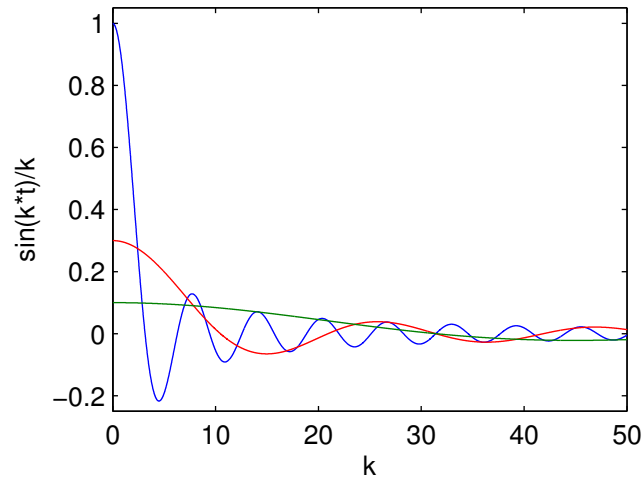Figure 3.1.: The weighting function Eq. (3.8) as a function of the wavenumber k for different times t. Blue: $t = 1.0$, red: $t = 0.3$, green: $t = 0.1$. Its first and most dominant peak becomes wider for smaller times t. This enters the following calculations through the kernel integral, Eq. (2.24), as the weighting function determines the contributing k-range of the Green's function.

small τ all frequencies contribute equally. The regime of small times τ is also the most important one to solve Eq. (2.23) since all later times will depend on it.

To describe this start-time limit appropriately, we use the Markov approximation. To do so it is necessary to split up the Green's function in a term describing the propagation in the medium and a term describing reflections, which form whenever the propagating electric field encounters a variation in the refractive index

$$\mathbf{G}(\mathbf{r}_A, \mathbf{r}_A, \omega) = \mathbf{G}^M(\mathbf{r}_A, \mathbf{r}_A, \omega) + \mathbf{G}^R(\mathbf{r}_A, \mathbf{r}_A, \omega). \tag{3.9}$$

The term featuring G^M is the solution of the Helmholtz equation with the (real) refractive index $n(x_A)$ of the medium the emitter is placed in, extended to infinity

$$\left(\Delta + n(x_A)^2 \frac{\omega^2}{c^2}\right) G^M(x, x', \omega) = \delta(x - x'). \tag{3.10}$$

The solution to this equation can be found analytically as follows

$$G^M(x, x, \omega) = \frac{ic}{2\omega n(x_A)}. \tag{3.11}$$

For the solution of G^M the refractive index was always evaluated at the same position x_A, accordingly the only difference between Eq. (3.11) and the vacuum Green's is the constant factor $1/n(x_A)$. Thus G^M can be treated very well in the Markov approximation. For the corresponding decay rate, Eq. (2.30), we get

$$\Gamma_0 = \frac{2k_A^2 \mu^2}{\hbar \epsilon_0} \frac{1}{2k_A n(x_A)} = \frac{k_A \mu^2}{\hbar \epsilon_0 n(x_A)}. \tag{3.12}$$

Following [9, 10] and our discussion in section 2.5 we omit the line shift $\delta\omega$, Eq. (2.29), as it describes a divergent contribution to the Lamb shift and can be thought of as being included in the transition frequency ω_A. The kernel, Eq. (2.24), then becomes

$$\overline{K}(t - t') = -\frac{\Gamma_0}{2} + \frac{\mu^2}{\hbar \pi \epsilon_0} \int_0^\infty d\omega \frac{\omega^2}{c^2} \left(\frac{e^{-i(\omega - \omega_A)(t - t')} - 1}{i(\omega - \omega_A)}\right) \operatorname{Im} G^R(\mathbf{r_A}, \mathbf{r_A}, \omega). \tag{3.13}$$

Using this kernel equation increases the accuracy for small times. This separation naturally works best in the vacuum or cavities with only very slight variations in the refractive index.

We demonstrate this for a dielectric slab such as in Fig. 4.1 with a refractive index $n_H = 1.01$ only slightly larger than the refractive index $n_L = 1.0$ of its surrounding medium[2]. The results for such a slab are shown in Fig. 3.1(a). In this case the

---

[2] All the geometries presented in this thesis are made up of two different refractive indices, a larger one, $n_{H(igh)}$, and a smaller one, $n_{L(ow)}$.

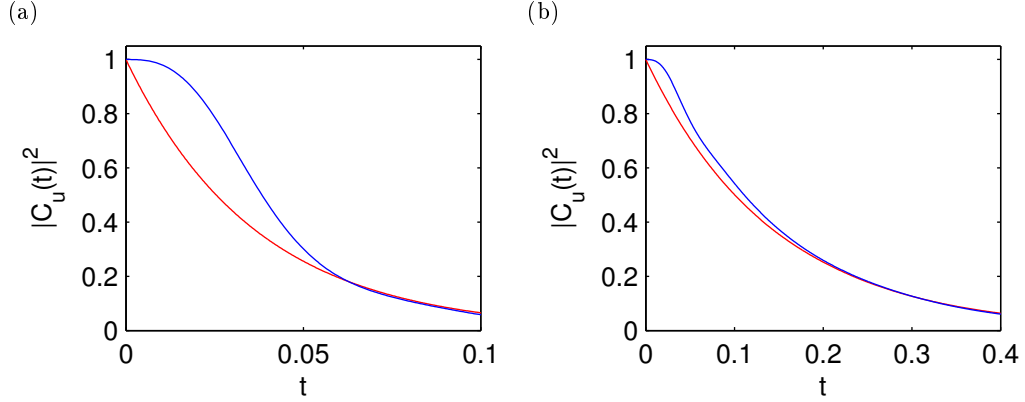(a)   (b)

Figure 3.2.: $|C_u|^2$ for a dielectric slab with refractive index $n_H = 1.01$ in (a) and $n_H = 4.0$ in (b) and length $l = 1.0$ placed in a medium with $n_L = 1.0$. Red: The Markov approximation was used for the G^M term and the kernel integral was solved for G^R. Blue: the kernel integral was solved for the total Green's function G. For small times a separate treatment of G^M and G^R is necessary to obtain the correct exponential decay.

total Green's function is almost identical to G^M, and thus G^R is negligible. The blue curves shows the result if G is not split up. The red curve illustrates the result when splitting up G, which is almost identical to the vacuum decay. It is well known that the spontaneous decay in the vacuum is described by an exponential decay. Obviously not splitting up G does not give the correct result for small times, but returns to the correct results for later times. This occurs because for $t = 0$ the kernel in Eq. (2.24) becomes zero, therefore the gradient of C_u is always zero at $t = 0$. Using Eq. (3.13) on the other hand yields $\overline{K}(0) = -\Gamma_0/2$ and produces the correct exponential decay. This error, when G is not split up, also occurs for larger refractive index variations, but is less prominent there (compare Fig. 3.1(a) with Fig. 3.1(b)).

3.2.2. Kernel

Before applying the separation of the Green's function from above, let us go back to the kernel integral derived in chapter 2.4,

$$\overline{K}(\tau) = \frac{\mu^2}{\hbar \pi \epsilon_0} \int_0^\infty d\omega \, \mathrm{Im}\, G(\mathbf{r}_A, \mathbf{r}_A, \omega) \left(\frac{e^{-i(\omega - \omega_A)\tau} - 1}{i(\omega - \omega_A)} \right) \frac{\omega^2}{c^2}. \qquad (3.14)$$

The real and imaginary part of this expression read

$$\operatorname{Re} \overline{K}(\tau) = \frac{\mu^2}{\hbar \pi \epsilon_0} \int_0^\infty d\omega \, \operatorname{Im} G(\mathbf{r}_A, \mathbf{r}_A, \omega) \left(\frac{-\sin(\omega - \omega_A)\tau}{\omega - \omega_A} \right) \frac{\omega^2}{c^2}, \qquad (3.15)$$

$$\operatorname{Im} \overline{K}(\tau) = \frac{\mu^2}{\hbar \pi \epsilon_0} \int_0^\infty d\omega \, \operatorname{Im} G(\mathbf{r}_A, \mathbf{r}_A, \omega) \left(\frac{-\cos(\omega - \omega_A)\tau + 1}{\omega - \omega_A} \right) \frac{\omega^2}{c^2}. \qquad (3.16)$$

In the one-dimensional systems we are considering, the Green's-function has a ω^{-1} behavior for high frequencies. Inserting for example the vacuum value $\operatorname{Im} G(\mathbf{r}_A, \mathbf{r}_A, \omega) = \frac{c}{2\omega}$ yields for the real and imaginary part of the kernel:

$$\operatorname{Re} \overline{K}(\tau) = -\frac{\mu^2}{2\hbar \pi \epsilon_0 c} \int_0^\infty d\omega \left(\frac{\omega}{\omega - \omega_A} \right) \sin((\omega - \omega_A)\tau), \qquad (3.17)$$

$$\operatorname{Im} \overline{K}(\tau) = \frac{\mu^2}{2\hbar \pi \epsilon_0 c} \left[\int_0^\infty d\omega \left(\frac{\omega}{\omega - \omega_A} \right) - \int_0^\infty d\omega \left(\frac{\omega}{\omega - \omega_A} \right) \cos((\omega - \omega_A)\tau) \right]. \qquad (3.18)$$

The real part contains an unspecified integral over a sine function. The imaginary part also contains an unspecified integral as well as a diverging term.

Splitting up the Green's function as discussed in section 3.2.1 does not avoid these problems. Although G^M, Eq. (3.11), is always positive and G^R therefore smaller than G, it does not decay stronger than $1/\omega$ for $\omega \to \infty$. The rest of this section is devoted to a correct treatment of the unspecified and diverging integrals in Eqs. (3.17) and (3.18).

Single Mode Approximation

In the single mode regime the emitter couples to only one mode of the cavity. The frequency of this cavity mode has to be very close to the transition frequency of the emitter. Hence the term ω^2/c^2 in Eq. (3.14) can be replaced, in good approximation, by k_A^2, see [10]. Doing so takes care of the problems induced by the undefined and diverging integrals in Eqs. (3.17) and (3.18).

As we are especially interested in the multi-mode coupling regime we, however do not make use of this approximation even for calculations where effectively a single-mode coupling is realized. In Fig. 3.2(a) and (c) we display the results in this multi-mode coupling regime using the single-mode approximation. The oscillations observed in $|C_u|^2$ start earlier than the return-time of the emitted photon and are therefore not physical. As a comparison we also show results of a correct treatment of the undefined integrals displayed in Fig. 3.2(b) and (d), which were obtained considering the Lamb shift and the finite volume of the emitter.
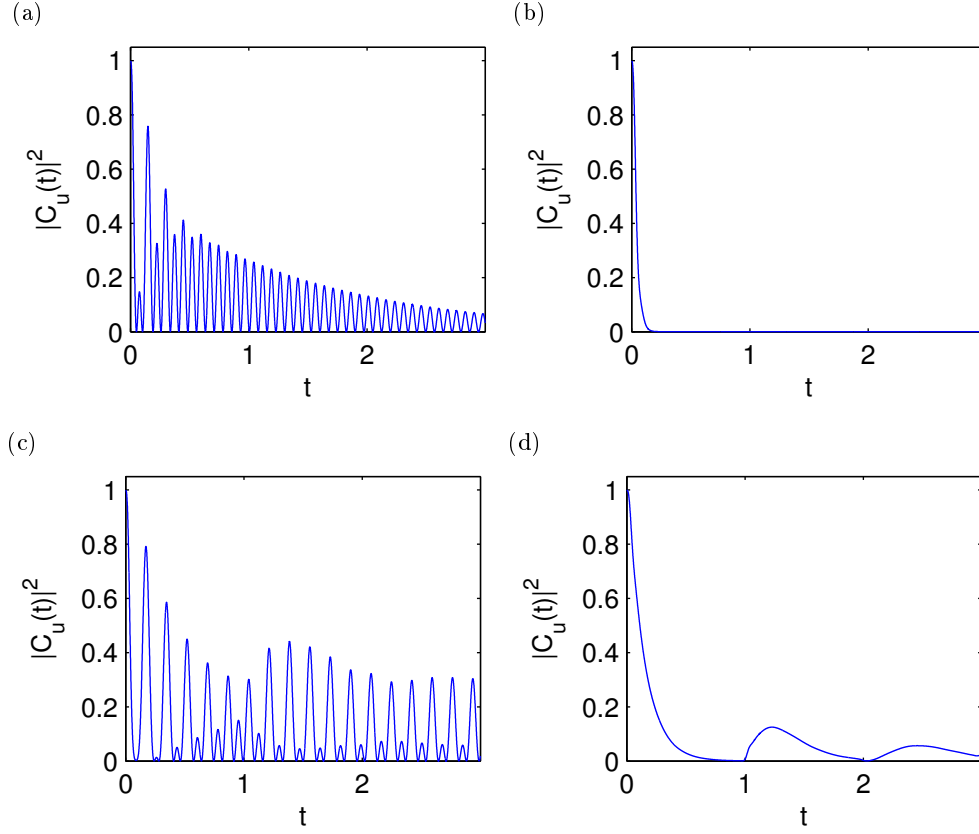
Figure 3.3.: Decay probability $|C_u|^2$ for a dielectric slab with refractive index $n_H = 1.01$ in (a), (b) and $n_H = 4.0$ in (c), (d) and length $l = 0.25$ placed in a medium with $n_L = 1.0$. The emitter with a dipole moment $\mu = 1$ is placed at $x_A = 0.125$ and has a transition frequency $k_A = 5\pi$. Figs. (a) and (c) are calculated using the single-mode approximation. The observed oscillations can not be correct, as they start earlier than the photon return time. Figs. (b) and (d) display the correct physical behavior without single-mode approximation. The first revival in (d) emerges at the photon return time. To obtain these results the contribution to the Lamb shift needs to be discarded and the finite size of the emitter has to be taken into account.

Lamb shift

When we applied the Markov approximation to the medium Green's function G^M, Eq. (3.11), we discarded the divergent line shift $\delta\omega$, Eq. (2.29), arguing it is part of the Lamb shift and already included in the transition frequency ω_A. We encounter a similar problem for the imaginary part of the kernel integral, Eq. (3.18), including the reflection Green's function G^R.

In the following paragraph we introduce the regularization of the Green's function, which takes care of the undefined real part of the kernel integral, Eq. (3.17). However, applying this method to the imaginary part of the kernel integral, Eq. (3.18), does not lead to meaningful results. The procedure we used for G^M, suggests to neglect the diverging Eq. (3.18) altogether. Our numerical calculations, presented in chapter 4, back up this procedure, as the obtained results can be explained very well with clear physical arguments.

Regularization of the Green's function

For the derivation of the central Eqs. (2.8), (2.23) and (2.24) the TLS was assumed to be point-like. This assumption is not justified in reality. The information about the size and position of the TLS does only implicitly enter the kernel integral, Eq. (2.24), via the Green's function. The Green's function $G(x_1, x_2, k)$ is a propagator of the electric field with the wavenumber k from position x_1 to x_2. In order to take the finite volume of the emitter into account, we use an average of the Green's function over both spatial dependencies instead of evaluating it only at the position x_A. After performing this averaging procedure an additional frequency dependent function $f(\omega)$ appears

$$\operatorname{Re}\overline{K}(\tau) = \frac{\mu^2}{\hbar\pi\epsilon_0} \int_0^\infty \mathrm{d}\omega \operatorname{Im} G(\mathbf{r}_A, \mathbf{r}_A, \omega) \left(\frac{-\sin(\omega - \omega_A)\tau}{i(\omega - \omega_A)} \right) \frac{\omega^2}{c^2} f(\omega). \quad (3.19)$$

In appendix C this function is calculated for the simplest case, i.e., in the vacuum with a Heaviside function to describe the volume of the emitter. For this simple case this function is

$$f(\omega) = \frac{\sin^2\left(\frac{\omega}{2}(b-a)\right)}{\left(\frac{\omega}{2}(b-a)\right)^2}. \quad (3.20)$$

Not only does this term take into account account the immediate vicinity of the TLS but it also removes the problem of the unspecified integral discussed in Eqs. (3.17). This term is of course in general only valid for the special case of the vacuum Green's function, but we observed that for all the systems we considered in this thesis, the envelope of the Green's function is $1/2k$. Hence we assumed that the general behavior of $f(\omega)$ also stays the same. The procedure to cut-off high frequency components in this way is known as "regularization" in the literature [18]. Different

ways exist to perform such a regularization [18, 19]. We choose for $f(\omega)$ a Gaussian function,

$$f(\omega) = \frac{e^{-(\omega-\omega_A)^2}}{2\sigma^2},$$
(3.21)

with a sufficiently large width σ which has the advantage of a sufficiently fast decay for high frequencies $\omega \to \infty$.

Summary of Kernel adaptations

In this chapter we discussed the necessary adaptations in Eq. (2.24) to solve Eq. (2.23) numerically. We have to split up the Green's function in a term G^M describing the propagation in the medium and a term G^R describing reflections. The propagation in the medium can be taken care off by applying the Markov approximation. For the reflection term further steps are necessary. The imaginary part of the weighting function has to be neglected and we added a Gaussian function to take care of the unspecified integral. The final equation for the kernel is

$$\overline{K}(\tau) = -\frac{k_A \mu^2}{2\hbar\epsilon_0 n(x_A)} +$$
$$+ \frac{\mu^2}{\hbar\pi\epsilon_0} \int_0^\infty d\omega \, \mathrm{Im}\, G(\mathbf{r}_A, \mathbf{r}_A, \omega) \left(\frac{-\sin(\omega-\omega_A)\tau}{\omega-\omega_A} \right) \frac{\omega^2}{c^2} \frac{e^{(\omega-\omega_A)^2}}{2\sigma^2}.$$
(3.22)

3.3. Numerical Methods

After the adaptations in the previous sections, the final Eqs. (2.8), (2.23) and (3.22) are obtained. In this chapter we will briefly discuss the numerical methods used to solve them.

3.3.1. Green's function

To calculate the Green's function we solve the Helmholtz Equation,

$$\left(\Delta + n(x,\omega)^2 \frac{\omega^2}{c^2} \right) G(x, x', \omega) = -\delta(x - x'),$$
(3.23)

by employing an equally spaced grid to discretize the geometry [20]. Discretization of the Laplacian gives

$$\frac{\partial^2}{\partial x^2} f(x) \bigg|_{x=x_n} \approx \frac{\frac{f_{n+1}-f_n}{\Delta x} - \frac{f_n-f_{n-1}}{\Delta x}}{\Delta x} = \frac{f_{n+1} - 2f_n + f_{n-1}}{(\Delta x)^2}.$$
(3.24)

The value of every grid point f_n depends on its neighboring grid points f_{n-1} and f_{n+1}. To employ Eq. (3.24) on the boundaries of the grid, we make use of the

$$-\partial_x f(x)\big|_{x=\frac{x_0+x_1}{2}} = ik\frac{f_0+f_1}{2} \qquad\qquad \partial_x f(x)\big|_{x=\frac{x_N+x_{N+1}}{2}} = ik\frac{f_N+f_{N+1}}{2}$$

Grid points

$0 \quad 1 \quad 2 \quad 3 \quad N-2 \;\; N-1 \quad N \quad N+1$

Δx

Figure 3.4.: An equally spaced grid is employed on the cavity and the finite difference method (FDM) is used. On the left and right side CF-boundary conditions are implemented to fix the flux out of the cavity

CF boundary condition shown in section 3.1, Eq. (3.3). It is important to choose the sign, such that the derivative, and therefore the flux, points out of the cavity, compare with Fig. 3.4. For the left end of the medium we get

$$-\partial_x f(x)\big|_{x=\frac{x_1+x_0}{2}} = \frac{f_0-f_1}{\Delta x} = ik\frac{f_0+f_1}{2} \qquad \rightarrow \quad f_0 = \underbrace{\frac{2+ik\,\Delta x}{2-ik\,\Delta x}}_{=\beta(k)}f_1, \qquad (3.25)$$

where we selected to not fix the value of the derivation at one grid point, but rather take the mean value of the last grid point inside the medium and the first adjacent grid point outside. Inserting this into the Laplacian yields

$$\frac{f_2-2f_1+f_0}{(\Delta x)^2} = \frac{1}{(\Delta x)^2}\left(f_2 + (-2+\beta(k))\,f_1\right). \qquad (3.26)$$

The Laplacian matrix with CF-boundary conditions then looks as follows

$$\frac{1}{(\Delta x)^2}\begin{pmatrix} -2+\beta(k) & 1 & & & & & \\ 1 & -2 & 1 & & & & \\ & 1 & -2 & 1 & & & \\ & & & \ddots & & & \\ & & & 1 & -2 & 1 & \\ & & & & 1 & -2 & 1 \\ & & & & & 1 & -2+\beta(k) \end{pmatrix}. \qquad (3.27)$$

Applying this method to the Helmholtz Eq. (3.23) provides a linear algebraic system of equations that can be solved with algorithms for tridiagonal matrices. For the grid size we always selected a uniform spacing Δx which was adapted for every wavelength λ, such that the relation $\Delta x < 30\lambda$ was always satisfied, for which good convergence can be expected.

This finite difference method can also applied for two- or three-dimensional systems. We mentioned in the beginning of this chapter, that, amongst other reasons,

we constrained our calculations to one-dimension because the numerical effort for higher dimensional systems increases strongly, as we need to obtain the Green's functions G and G^R, for a large range of wavenumbers k.

3.3.2. Kernel Integral

The integral to calculate $\overline{K}(\tau)$, Eq. (3.22), was solved using the trapezoidal rule. Delicate questions in this context are the proper spacing of the wavenumber k and where to cut off the integral. There are two factors influencing the k-spacing. On the one hand it needs to resolve all the peaks in the Green's function, on the other hand it also needs to resolve the oscillations of the weighting function[3] which especially becomes a problem for long times. In certain cases these two requirements demanded numerically challenging configurations, such as a small step-width and a large range of integration. The results presented in this thesis can be obtained for a justifiable computational effort, while fulfilling these requirements. For more demanding configurations a separated calculation of the Green's function and the weighting function might be useful.

To calculate $C_u(t)$ we used an algorithm with adaptive step width, which requires that the integrand in the Volterra equation (2.23) can be evaluated for any time $t' \in [0, t]$. We made this possible by using a Matlab routine to generate a cubic spline of the kernel function. $K(\tau)$ is essentially the Fourier transform of the Green's function, hence $2\pi/k_{\max}$ would be an obvious choice for the step-width $\mathrm{d}\tau$. This value turned out to be too coarse to get stable results, which were eventually obtained by refining the step-width by two orders of magnitude.

3.3.3. Volterra Integral Equation

As mentioned before we used the trapezoidal rule [21] with variable step width to solve the Volterra integral equation [22]. The advantage of this method is that it allows us to specify a limit for the relative error and the minimum step width. The steps will be chosen as large as possible with the relative error staying below the specified limit. In case that the desired limit for the relative error can not be reached the minimum step width is used. For more details we refer to appendix D.

---

[3] This is the function multiplied with the Green's function in Eq. (2.24). Its importance is discussed in chapter 4.

Chapter 4.

Results

4.1. Dielectric Slab

The first system we consider is that of a slab with length l and a constant refractive index n_H surrounded by a medium with a lower refractive index n_L, see Fig. 4.1. We placed the TLS in the center of the slab and thus need to calculate $\operatorname{Im} G(l/2, l/2, k)$. When the imaginary part of G is plotted as a function of the wavenumber k, there are peaks visible representing the resonances of the cavity. The position of these peaks can be calculated by simply adding up the different possible paths in the slab. All the possible paths starting from the position of the TLS and propagating back to the starting position are

$$t = e^{inkL/2}\, r\, e^{inkL/2} + \left(e^{inkL/2}\, r\, e^{inkL/2}\right)^2 + \dots$$

$$= \sum_{n=1}^{\infty} r\, e^{inkL} = \frac{r\, e^{inkL}}{1 - r\, e^{inkL}}. \tag{4.1}$$

Paths to the left and right actually have to be treated separately in general, but here we assumed that emission to the left and right is equally probable. Thus each term has an additional factor $1/2$, but as each path has an identical mirror-image this factor cancels out again. The reflection coefficient $r = (n_H - n_L)/(n_H + n_L)$ is greater zero. Therefore the transmission has maxima for $nk_m L = 2\pi m$. These
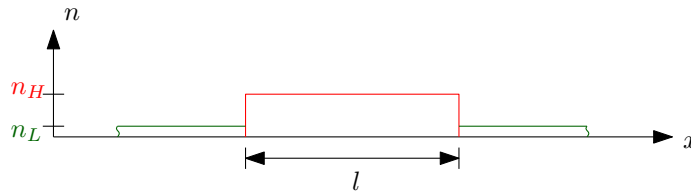
Figure 4.1.: A dielectric slab (red) with refractive index n_H placed in a medium with refractive index n_L. This system with an emitter placed in the center of the slab is discussed in section 4.1
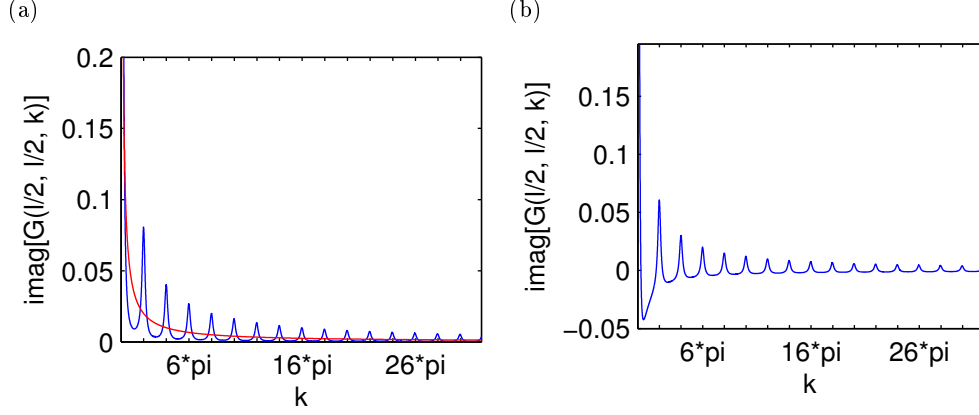
Figure 4.2.: The Green's function of a dielectric slab (Fig. 4.1) with $n_H = 4.0$, $n_L = 1.0$ and $l = 0.25$. (a): The total Green's function G (blue) and the medium Green's function $G^M = 1/(2k_A n_H)$ (red). (b): Reflection Green's function $G^R = G - G^M$. The peaks of G in (a) and G^R in (b) indicate the cavity resonances, they occur for $k_m = 2\pi m/(n_H l) = 2\pi m$.

maxima can be identified in the total Green's function G, shown in Fig. 4.1(a), as well as in the reflection Green's function G^R, shown in Fig. 4.1(a).

As mentioned in chapter 3.1, another way to determine the resonance frequencies of a cavity is to look at the CF eigenvalues. In Fig. 4.3 the CF eigenvalues for a certain range of k-vectors is displayed. The real part of the eigenvalues is relatively stable. Especially in the chosen k-range, the $k_m(k)$ are almost vertical straight lines. The spacing of the $\operatorname{Re} k_m(k)$ is $m\pi/L$, the same as in a potential well. In the Green's function, however, only peaks for odd m are found. This is because the TLS was placed in the center of the cavity. The CF states with even m are zero at $x = l/2$, therefore these resonances do not appear in the Green's function. The CF eigenvalues do not only contain information about the frequency of the cavity modes, also their imaginary part is a measure of how well they are trapped in the cavity. The red dots in Fig. 4.3 mark the CF eigenvalues $k_1(k)$ closest to the wavenumber k they were calculated for (we indicate this by using the index 1 for these eigenvalues). This was done for 7 different resonance frequencies of the slab. For increasing k the absolute value of the imaginary part of the $k_1(k)$ increases slightly. The bigger k gets, the weaker the CF states are bound, although the differences are very small on an absolute scale.

So far we know the modes of the cavity and have a measure of how well they are bound. The next question is to which of these modes the TLS couples. Comparing the reflection Green's function G^R with the weighting function Eq. (3.8) which is
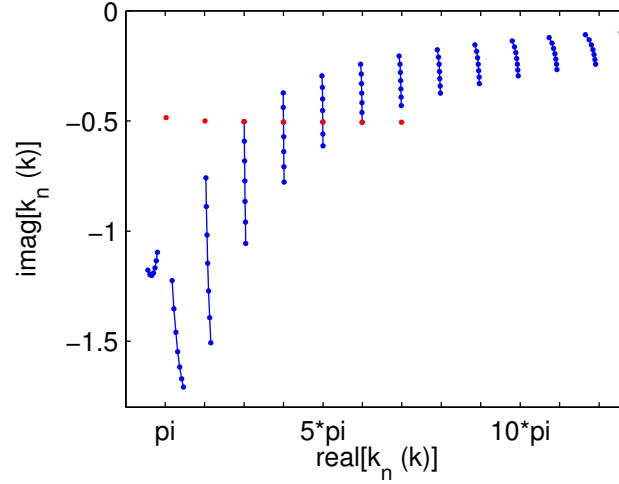
Figure 4.3.: CF eigenvalues of a dielectric slab (Fig. 4.1) with $n_H = 4.0$, $n_L = 1.0$ and $l = 0.25$. Each blue line indicates a CF eigenvalue $k_m(k)$ in the wavenumber interval $k \in [3\pi, 6\pi]$. The eigenvalues calculated for $k = 3\pi, 3.5\pi, 4\pi \ldots 6\pi$ (indicated by the blue dots). The red dots display the CF eigenvalue $k_1(k)$ closest to the respective k, calculated for $k = \pi, 2\pi \ldots 7\pi$.

multiplied with G in Eq. (3.22) gives an estimate of how many modes need to be taken into account. Consider as an example Fig. 4.3(a) where the main peak of the weighting function spans over 2 modes. To evaluate the weighting function it is necessary to insert a value for the time τ. In all the results presented in this thesis we chose the value $\tau = 1/(3\Gamma_0)$. The factor $1/3$ is arbitrary, but it is practical to make τ a multiple of $1/\Gamma_0$ because it is a measure for the time scale of the system specific dynamics. This way it can be used to compare the coupling characteristics of different systems. Note that the weighting function is also scaled by a global factor in most figures to facilitate a comparison with G. As mentioned earlier the width of the weighting function depends on the time t. The time scale of the decay, in turn, depends strongly on the kernel. As is easy to understand in the vacuum, the bigger $|\Gamma_0|$ gets, the faster C_u decays. The absolute size of the kernel depends mostly on the prefactor $k_A^2 \mu^2/(\hbar \pi \epsilon_0)$ in Eq. (3.22). Besides the constants and the transition frequency k_A (which for our purposes always stays in the same order of magnitude) there is only one parameter that is variable, which is the dipole moment μ. Hence the dipole moment μ can be seen as a coupling constant, describing how strong the emitter couples to the cavity modes. The bigger μ gets, the bigger becomes the kernel and the smaller the time scale of the dynamics in C_u. Also for small times t there are more frequencies of G (respectively G^R) contributing to the kernel because

the weighting function Eq. (3.8) gets wider. In a nutshell this tells us that for a small enough coupling constant μ the TLS couples to only one mode, and for big enough μ the system is in the multi-mode coupling regime.

The next step is the calculation of the kernel, Eq. (3.13). For a TLS placed in the center of the cavity, the return-time, that is the minimal time for the emitted photon to return to the TLS, is $c\,2\,l/2 = 1$ (in the geometry chosen here). The steps in the kernel (Fig. 4.3(b)) occur around integer multiples of the return-time. In between these steps the kernel is more or less constant. The characteristics of the kernel translate into the occupation probability of the upper state $|C_u|^2$. In the time intervals in which the kernel is approximately constant and smaller than zero an exponential decay can be observed in $|C_u|^2$ (Fig. 4.3(c)). The steps in the kernel produce revivals in $|C_u|^2$, such that the photon is reabsorbed by the emitter. Looking at the results for G, $\overline{K}$ and $|C_u|^2$ for the example in Fig. 4.4 it is easy to see that the weighting function Eq. (3.8) spans over a large frequency range and therefore the emitter couples to many modes.

In the remainder of this section we will present the results of a slab with $n_H = 4.0$, $n_L = 1.0$ and length $l = 1.0$. We show the influence of the dipole moment μ on the basis of this geometry. Again the TLS is placed in the center $x_A = 0.5$ and the emitter frequency is $k_A = 5\pi$, which corresponds to the 10th resonance of the slab ($2\pi m/(nL) = \pi m/2 = 5\pi$ for $m = 10$). In Figs. 4.5, 4.6 and 4.7 the reflection Green's function G^R and C_u is displayed. The Green's function, compared with the weighting factor Eq. (3.8) gives a picture of how many modes the emitter couples to.

First we discuss a small enough value for μ to couple to only one resonance of the Green's function. The single coupling behavior is easy to see in Fig. 4.4(a). The weighting function is only significant within the one peak of G^R around k_A. In the geometry we are using here, all the modes are bound equally well. For the used values n_H and n_L the classical reflection at the cavity boundaries is rather small

$$R = \left| \frac{n_H - n_L}{n_H + n_L} \right|^2 = \left| \frac{3}{5} \right|^2 = \frac{9}{25} = 0.36 \ , \tag{4.2}$$

making it is very unlikely for the emitted photon to stay in the slab for more than a few round-trips (e.g. $R^3 = 4.7\%$). Also due to the small dipole moment the Markov decay Γ_0 is very low. With the dwell time of the photon so low compared to the time scale of the Markov decay, the chance of reabsorption is negligible. Figure 4.4(b) confirms this as C_u is simply described by an exponential decay, slightly stronger than the Markov decay.

In Fig. 4.6 the dipole moment μ is increased by one order of magnitude. There are two interesting phenomena to observe in this case. For one it is clearly visible that up to the return time $t_r = c\,l/2\,n\,2 = 4$ the decay is exactly the Markov decay.
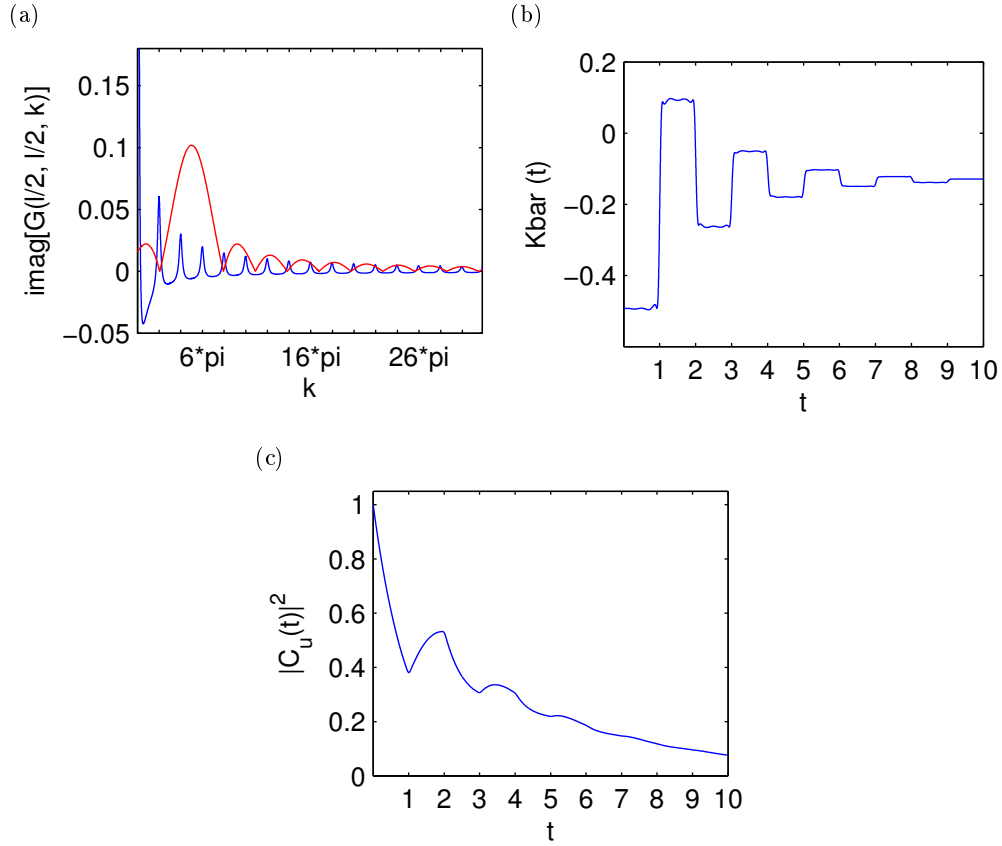
Figure 4.4.: Results for for a dielectric slab: $n_H = 4.0$, $n_L = 1.0$, $l = 0.25$, $k_A = 5\pi$, $x_A = 0.125$, $\mu = 0.5$. (a): The Reflection Green's function G^R (blue) compared with the weighting function $|\frac{\sin((k-k_A)/(3\Gamma_0))}{k-k_A}| * 0.3$ (red) indicates that the system is in the multi-mode coupling regime. (b): The kernel function $\overline{K}(t)$, Eq. (3.22), with steps occurring at integer multiples of the photon return time $t_r = c\,n_H\,l = 1$. (c): The upper state occupation probability $|C_u(t)|^2$, Eq. (2.23), with revivals caused by the steps in the kernel.
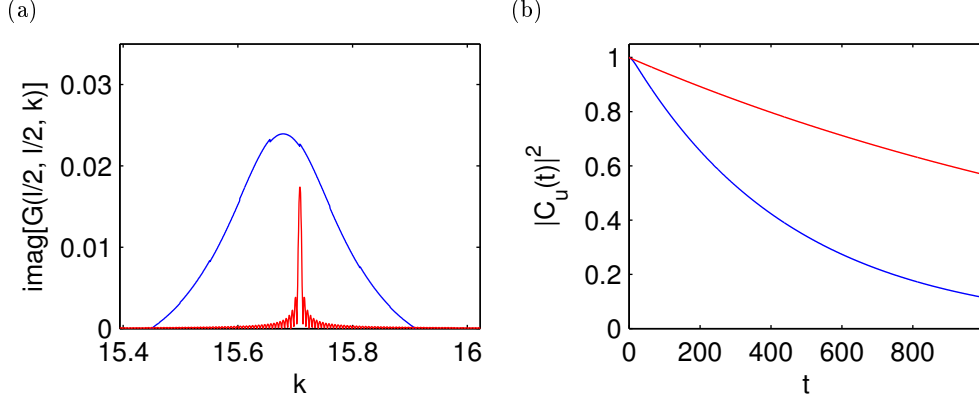
Figure 4.5.: Results for a dielectric slab: $\mu = 0.012$, $n_H = 4.0$, $n_L = 1.0$, $l = 1.0$, $x_A = l/2$, $k_A = 5\pi$. (a): The reflection Green's function G^R (blue) and the weighting function $|\frac{\sin((k-k_A)/(3\Gamma_0))}{k-k_A}| * 3 * 10^{-5}$ (red). The TLS couples to only one mode. (b): $|C_u(t)|^2$ describes an exponential decay, that is enhanced compared to the Markov decay $\exp(-\Gamma_0 t)$ (red). This represents weak coupling within the single-mode coupling regime.

This is also the case in Fig. 4.4(b) but due to the larger time scale not visible in the according plot. Furthermore $|C_u|^2$ is not monotonically decreasing anymore. After an initial exponential decay, there appears a small revival in $|C_u|^2$. The plot of G^R still shows that the cavity mode closest to k_A has the biggest influence, but the contribution of the adjacent modes is not negligible anymore. This also explains why $|C_u|^2$ is not a simple exponential decay any longer. The dipole moment is larger and therefore couples more strongly to the cavity resonances, which manifests in a faster decay of the TLS. So while the decay is enhanced due to the increased dipole moment, the dwell time of the photon in the cavity stays the same, which means that the chance for the photon to stay in the cavity for the duration of the decay is much larger than compared to the earlier example. Hence there is a higher chance of reabsorption.

Finally we increase the dipole moment once again by a factor 10. Now the system is clearly in the multi-mode coupling regime as the weighting function in Fig. 4.6(a) now spans over a large frequency range. The high dipole moment causes the TLS to couple very strongly to the cavity modes, so the probability of spontaneous emission earlier than the return time is almost one. Now the effect we already observed for a dipole moment one order of magnitude smaller is even more prominent. The decay is very fast, so there is interaction between the TLS and many cavity resonances. The characteristics of C_u (Fig. 4.6(b)) can be explained in a quasi-classical picture.
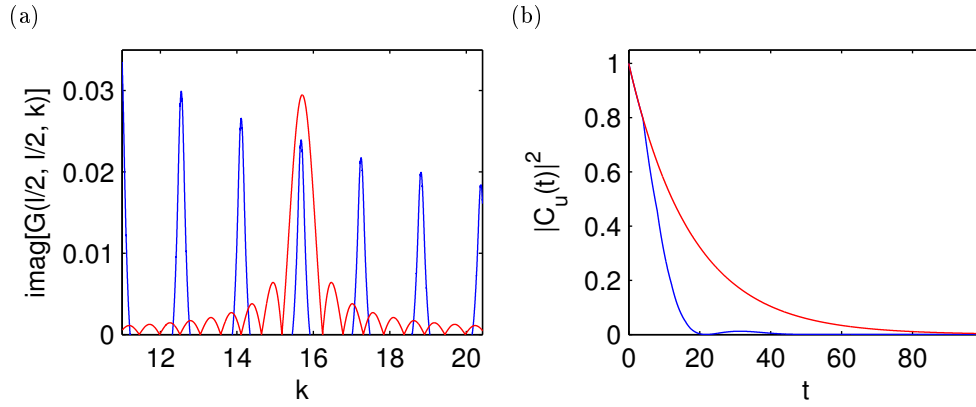
(a)

(b)
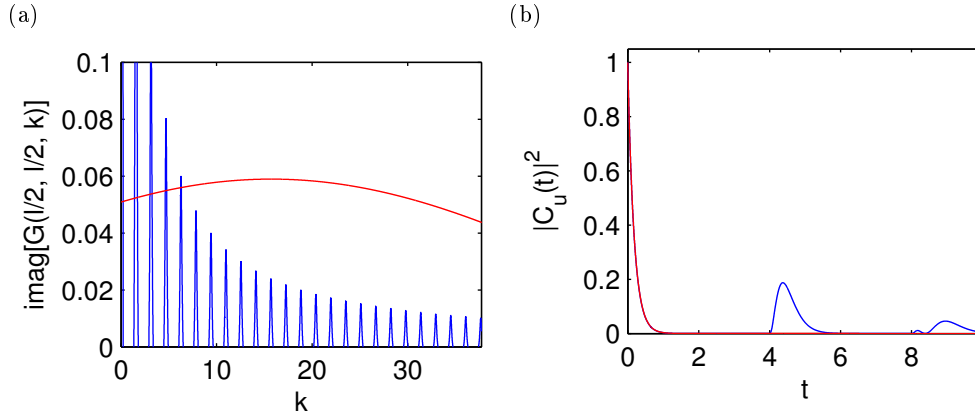

Figure 4.6.: Results for a dielectric slab: $\mu = 0.12$, $n_H = 4.0$, $n_L = 1.0$, $l = 1.0$, $x_A = l/2$, $k_A = 5\pi$. (a): The reflection Green's function G^R (blue) and the weighting function $|\frac{\sin((k-k_A)/(3\Gamma_0))}{k-k_A}| * 5 * 10^{-3}$ (red). The TLS mainly couples to the closest resonance, but also starts coupling to other modes. (b): $|C_u(t)|^2$ (blue) corresponds to the Markov decay $e^{-\Gamma_0 t}$ (red) up to the cavity return time $t_r = 1$. For larger times an enhanced decay is observed, with one very small oscillation visible. The system is in the few-mode coupling regime.

(a)   (b)

Figure 4.7.: Results for a dielectric slab: $\mu = 1.2$, $n_H = 4.0$, $n_L = 1.0$, $l = 1.0$, $x_A = l/2$, $k_A = 5\pi$. (a): The weighting function $|\frac{\sin((k-k_A)/(3\Gamma_0))}{k-k_A}|$ (red) spans over many modes of G^R (blue). (b): $|C_u(t)|^2$ (blue) follows the Markov decay $e^{-\Gamma_0 t}$ (red) up to the cavity return time $t_r = 1$ and then shows a quasi-classical behavior. The system is in the many-mode coupling regime.

The photon is emitted almost instantly and bounces back and forth between the walls of the slab a few times and every time it passes the emitter there is a chance to get reabsorbed, an effect which manifests itself in the peaks of C_u. Of course these peaks decrease in size quite fast, because the reflection is not very high in the dielectric slab ($R = 36\%$ for $n_H = 4$ and $n_L = 1$).

In this section we have discussed the characteristic of Eqs. (3.13) and (2.23) on the basis of a simple geometry, i.e. a dielectric slab with constant refractive index n_H (Fig. 4.1). A crucial parameter in the system is the dipole moment μ which determines the time scale of the dynamics of the system and hence the characteristics of C_u. We see however, that as we scan the dipole moment from weak to strong coupling Rabi oscillations only occur with very low amplitude and for well-defined parameter values. To observe Rabi oscillations in a more pronounced way, we consider a cavity with a $\lambda/4$-layer at its boundaries.

4.2. $\lambda/4$ Layer

One way to increase the dwell time of a selected mode in the cavity is to add so-called $\lambda/4$ layers on each side, see Fig. 4.7(b). To achieve the desired effect, the first refractive index transition has to be from a lower to a higher value. That is why the central slab is a medium with n_L now. Connected to it are thin layers with
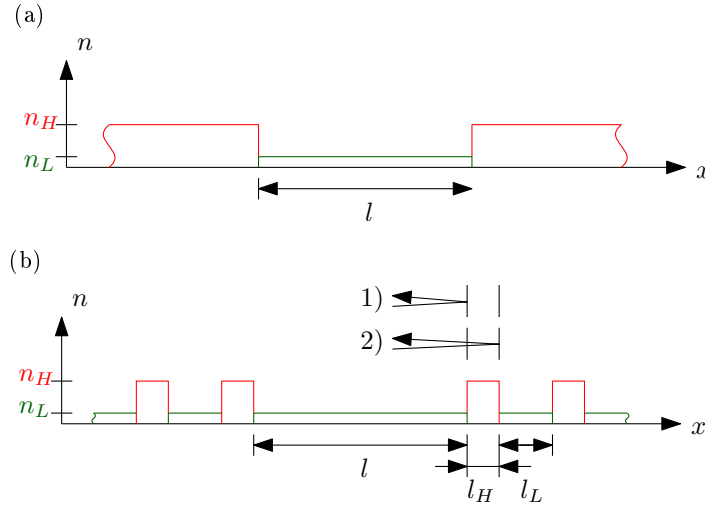
Figure 4.8.: (a): A slab with a low refractive index n_L and a high refractive index n_H to its left and right. (b): The reflection of a specified wavelength is increased by adding $\lambda/4$-layers on both sides. Choosing $n_H l_H$ and $n_L l_L$ accordingly, allows for constructive interference of the reflected beams.

alternating high, n_H, and low, n_L, refractive indices. Each one of these thin layers is called a $\lambda/4$ layer. We used three $\lambda/4$ layers (two with high and one with low refractive index), which provided a high enough reflection for our purposes.

The functionality of $\lambda/4$ layers is quite easy to explain. The thickness of the n_H and n_L layers have to be chosen correctly, so the two reflected beams interfere constructively for a specified wavelength. The first beam, reflected on the n_H-layer acquires a phase-shift of π (because we always chose $n_H > n_L$). The second beam is shifted by kL in respect to the first beam (it does not accumulate a shift during the reflection, since $n_L < n_H$). Hence the condition for maximal reflection is

$$\left.\begin{array}{ll} 1) & e^{i\pi} \\[2mm] 2) & e^{ikL} = e^{i\frac{2\pi}{\lambda}2nd} \end{array}\right\} \qquad \frac{4\pi}{\lambda}\underbrace{nd}_{=\frac{\lambda}{4}} = \pi. \tag{4.3}$$

Obviously this condition can only be fulfilled for one wavelength at a time (and integer multiples of it). To demonstrate the effect of these $\lambda/4$ layers we look at the Green's function of a slab with length l and refractive index n_L. To its left and right is a medium with refractive index n_H (see Fig. 4.7(a)). We compare this system to a system with the same length l and two $\lambda/4$-layers on each side like in Fig. 4.7(b). We compared the Green's function of these two systems as a function of the wavenumber k. Again the emitter is placed in the center $x_A = l/2$.

In Fig. 4.8(a) the Green's function of the system without $\lambda/4$-layers is shown. The position of the peaks is explained the same way as in section 4.1 using path summation Eq. (4.1), except this time $r = (n_L - n_H)/(n_L + n_H)$ is negative and the condition for maximal transmission becomes $nk_m l = 2\pi(m + 1)$. Accordingly, the peak spacing is still 2π (for $n_L = 1$ and $l = 1$) but the peaks are now located at odd multiples of π. In Fig. 4.8(c) the Green's function of the system with $\lambda/4$-layers is displayed. The thickness of the layers was chosen such that

$$nd = \frac{\lambda_A}{4} \quad \text{for} \quad k_A = \frac{2\pi}{\lambda_A} = 5\pi \tag{4.4}$$

was fulfilled. We picked the value 5π for k_A so it coincides with a peak of the Green's function. Therefore the eigenvalue $k_m = k_A$ and whole-number multiples of k_A are amplified, as well as the adjacent peaks.

The plots of the Green's function of the system with and without $\lambda/4$-layers already show the effect of the enhanced reflection. However, we also look at the CF eigenvalues of these two systems (Fig. 4.10). The CF eigenvalues of the slab without $\lambda/4$-layers show similar characteristics as compared to what we have seen already in section 4.1. Again the functions $k_m(k)$ are almost vertical straight lines. The red dots indicate the CF eigenvalue closest to the wavenumber k for which they were calculated. The imaginary parts of these eigenvalues increase very slightly with increasing k. Yet the CF eigenvalues are strongly modified when the $\lambda/4$-layers are added. The geometry was designed to trap the transition frequency of the TLS for a long time in the cavity. The corresponding eigenvalue is very close to the real axis, as well as the adjacent eigenvalues. The other eigenvalues are also distorted quite strongly, but this effect does not have a strong influence on the Green's function.

After comparing these two systems we want to focus in the following only on the system with the $\lambda/4$-layers. Using its reflection Green's function (Fig. 4.8(c)) we solve Eqs. (2.23) and (3.22) to calculate the occupation probability of the upper state $|C_u(t)|^2$. Again the dipole moment μ is a crucial parameter in these calculations, as it is a coupling constant of the TLS to the electric field. The following sections show results for the $\lambda/4$ geometry in different coupling regimes.

4.2.1. Single-mode coupling

Like for the simple slab, the system is in the single coupling regime for small dipole moments. Figure 4.10(a) shows the same characteristics as we have already seen for systems without enhanced reflection. The TLS decays faster than the Markov decay, but still on a time scale much bigger than the return time of the photon.

The impact of the $\lambda/4$-layers becomes first visible for Fig. 4.10(b). Instead of an exponential decay we observe damped oscillations. This is because the $\lambda/4$-layers were designed to enhance the reflection of the resonance mode which is in tune with
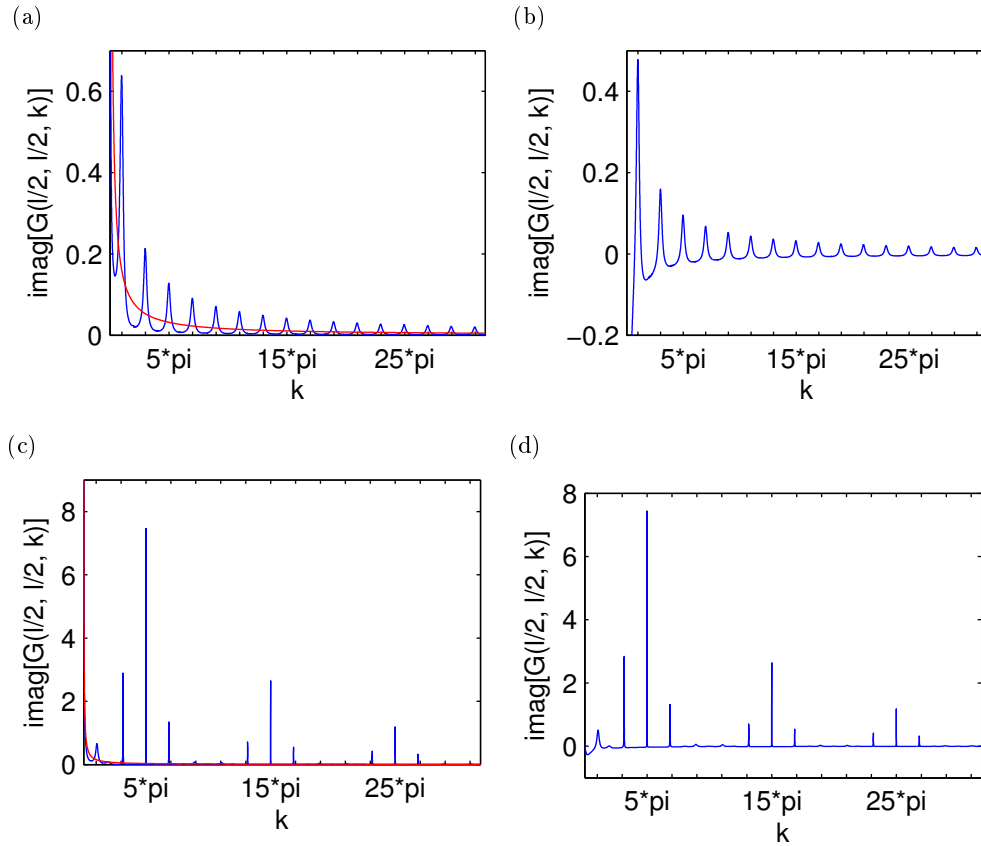
(a)

(b)

(c)

(d)

Figure 4.9.: Comparison of the Green's function two systems. In (a) and (b) a dielectric slab ($l = 1.0, n_L = 1.0, n_H = 4.0$) like in Fig. 4.7(a) was considered, whereas in (c) and (d) $\lambda/4$-layers ($l_H = 0.025, l_L = 0.1$) were added, see Fig. 4.7(b). In (a) and (c) the total Green's function G (blue) and the medium Green's function G^M (red) is plotted for the respective systems. Figs. (b) and (d) show the reflection Green's function $G^M = G - G^R$. The frequencies for which the $\lambda/4$-layers were designed are strongly amplified. Notice the different length scales of the y-axis.
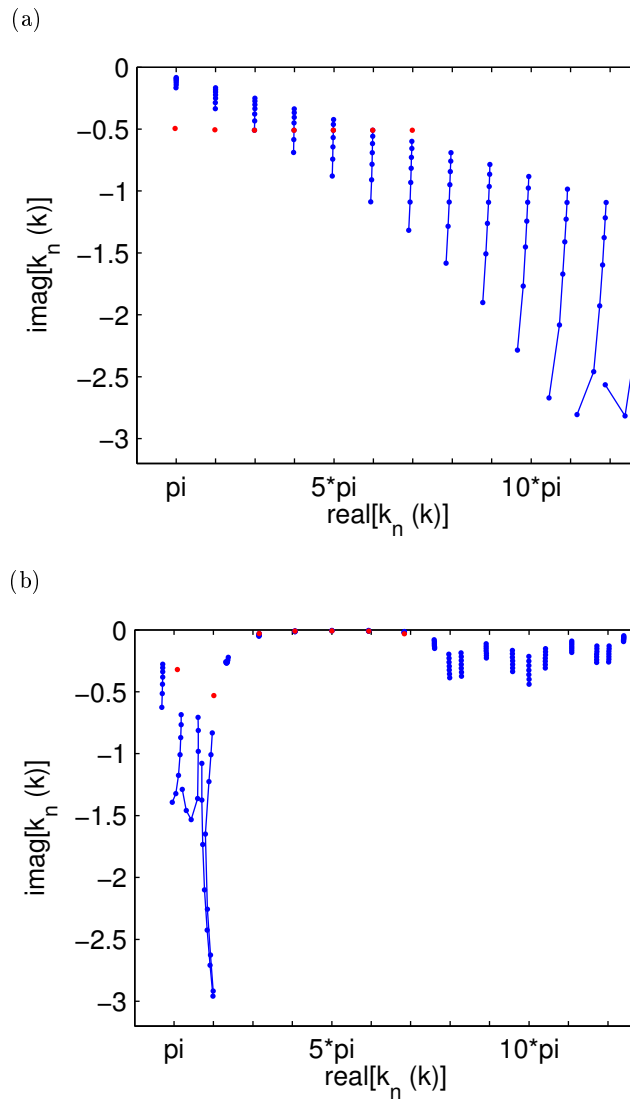
(a)

(b)

Figure 4.10.: CF eigenvalues for two different geometries: (a) is the same system as in Figs. 4.8(a), 4.8(b) and (b) is the same system as in Figs. 4.8(c), 4.8(d). Each blue line indicates a CF eigenvalue $k_m(k)$ in the wavenumber interval $k \in [3\pi, 6\pi]$. The eigenvalues were calculated for $k = 3\pi, 3.5\pi, 4\pi \ldots 6\pi$ (indicated by the blue dots). The red dots display the CF eigenvalue $k_1(k)$ closest to the respective k, calculated for $k = \pi, 2\pi \ldots 7\pi$. The CF eigenvalues of the system with the $\lambda/4$-layers are much closer to the real axis and, thus, have a longer dwell time in the cavity.
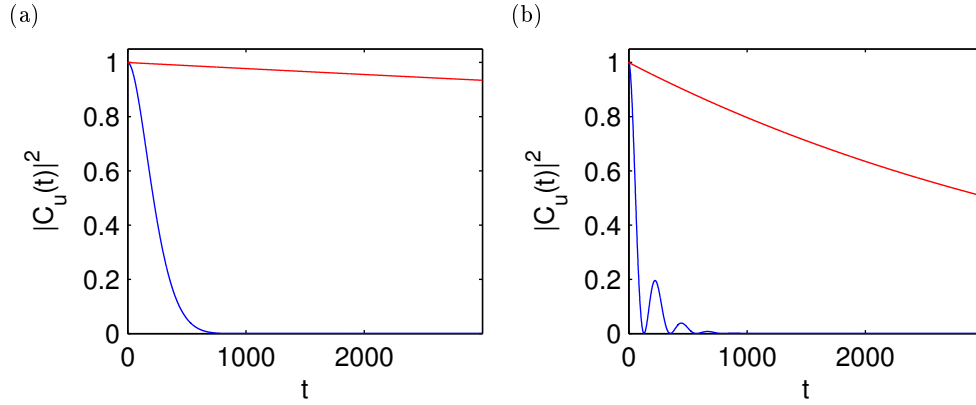
Figure 4.11.: $|C_u(t)|^2$ for a geometry like in Fig. 4.7(b) with $l = 1.0, n_H = 4.0, l_H = 0.025, n_L = 1.0$ and $l_L = 0.1$. The emitter is placed in the center of the slab $x_A = 0.5$ and has a transition frequency $k_A = 5\pi$. Two different dipole moments, $\mu 0.0012$ in (a) and $\mu = 0.0038$ in (b), are taken into account. For the larger value of μ weak Rabi oscillations are visible.

the TLS transition frequency. Compared to the single-mode coupling of the regular slab, the system still couples with only one mode, but the dwell time of this mode is strongly increased. This induces a longer time of interaction between the emitter and the respective cavity resonance. The emitter does not simply decay, but there is also a chance of reabsorption of the photon, which causes the mentioned oscillations. This phenomenon is called Rabi oscillations and is a well known effect in the strong coupling regime of single mode cavities [9].

In the next example we included the plot of the Green's function compared with the corresponding kernel weighting function (Fig. 4.11(c)) in the same fashion as in the last section. This illustrates that the system is still clearly in the single-mode coupling regime for the according dipole moment μ and, thus, also for the systems shown Figs. 4.10(a) and 4.10(b), as they have an even smaller dipole moment. The larger dipole moment in Fig. 4.11(b) compared to Fig. 4.10(b) causes a stronger coupling of the TLS to the cavity mode and therefore a faster decay is observed. The oscillations take place on a smaller time scale and, as the dwell time of the resonance is the same, they do not decay as fast compared to the respective Markov decay. This is why Fig. 4.11(b) displays such distinct Rabi oscillations.

To observe Rabi Oscillations in the model we use, the dipole moment can not get too large, otherwise the emitter will couple to more than one mode. On the other hand the coupling needs to be relatively strong while staying in the single coupling regime. This lower limit for the dipole moment is necessary, so the emission of
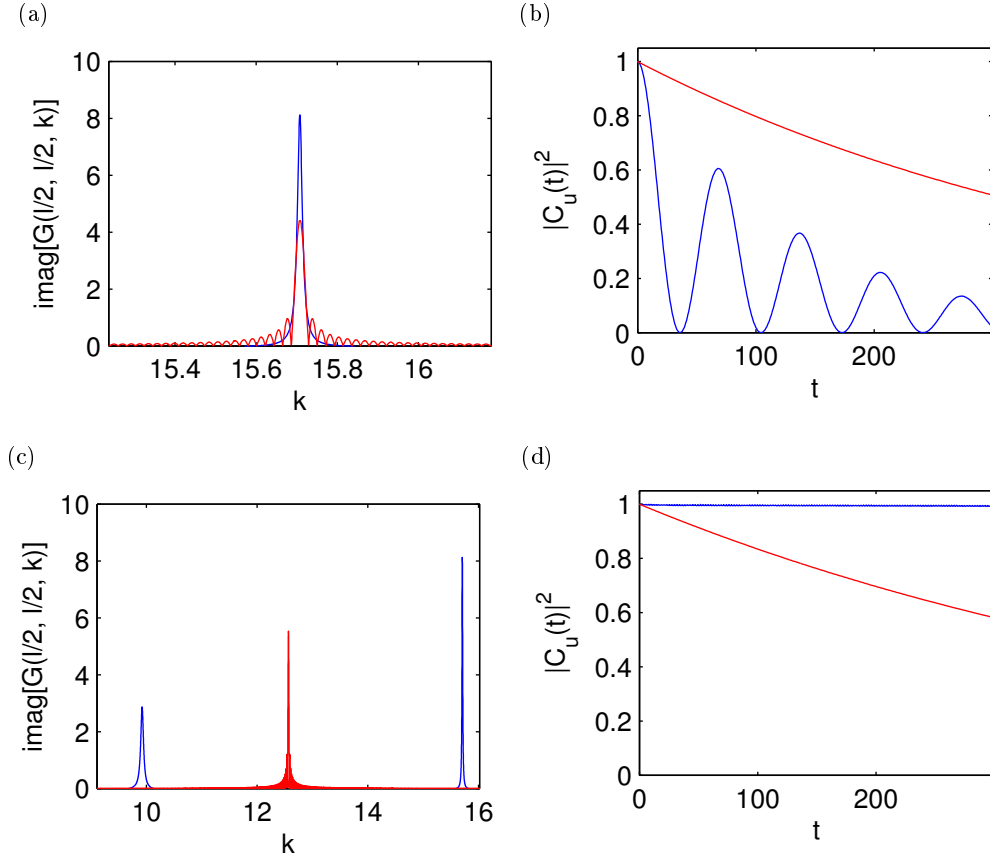
(a)

(b)

(c)

(d)

Figure 4.12.: The same system as in Fig. 4.11 is considered with a different dipole moment $\mu = 0.012$ and the transition frequency is tuned off resonance in (c) and (d) $k_A = 4\pi$. In (a) and (c) G^R (blue) and the weighting function $|\frac{\sin((k-k_A)/(3\Gamma_0))}{k-k_A}| * 0.03$ (red) are displayed. The TLS couples to one cavity mode in (a) and does not couple to any cavity modes in (c). Thus, for $|C_u|^2$ we observe Rabi oscillations in one case (b) and no interaction at all in the other (d).

the photon happens considerably fast compared to the dwell time of the resonance. That is why we needed to increase the dwell time of the resonance the TLS couples with. We want to discuss the impact of the $\lambda/4$-layers on the basis of the results for the system with $\mu = 0.012$ in Fig. 4.11(b). The reflection probability for a transition from a refractive index $n_L = 1.0$ to $n_H = 4.0$ is

$$R = \left(\frac{n_L - n_H}{n_L + n_H} \right)^2 = 36\%. \tag{4.5}$$

To calculate the reflection probability at $\lambda/4$-layers multiple reflections need to be considered. A correct derivation [23] yields for a wavenumber k_A the reflection

$$R(\lambda_A) = \frac{n_H^4 - n_L^4}{n_H^4 + n_L^4} = 99.22\%. \tag{4.6}$$

It takes the photon the time $t = c\,l = 1$ to travel once through the cavity. The first maximum of the Rabi oscillations occurs in Fig. 4.11(b) approximately at $t = 68$ and the second one at $t = 137$. So at the time of the first maximum the photon traveled 68 times back and forth in the cavity (respectively 137 times at the second maximum). The chance for the photon to remain that long in the dielectric slab is with

$$R^{68} = 0.36^{68} = 6.7 * 10^{-29}\%, \qquad R^{137} = 0.36^{137} = 1.6 * 10^{-59}\% \tag{4.7}$$

only negligible small. This is why there were no Rabi oscillations visible in Fig. 4.4(b). It is not possible to fulfill both requirements, that is being in the single mode coupling regime while coupling strong enough to that one mode, at the same time[4]. With the $\lambda/4$-layers on the other hand the reflection is

$$R^{68} = 0.9922^{68} = 58.71\%, \qquad R^{137} = 0.9922^{137} = 34.21\%, \tag{4.8}$$

which fits very well with the height of the maxima in Fig. 4.11(b).

All the results so far, were engineered such that the transition frequency coincides very well with a cavity mode. We have not discussed the detuning Δ at all, i.e., the difference between the transition frequency ω_A and the closest resonance ω_m. An example with maximal detuning is illustrated in Fig. 4.11(c), (d), which is the same system as in Fig. 4.11(a), (b), except for the transition frequency of the TLS, which is placed right in the middle between two resonances. For the given dipole moment, the coupling is not strong enough to allow an interaction even with the closest field mode, causing the emitter to remain in the exited state, Fig. 4.11(d). This can also be understood analytically. There is no significant overlap between the Green's function G and the weighting function in Fig. 4.11(c), thus the kernel is zero for all times and C_u retains its initial value.

---

[4] Unless for unrealistic high differences between the refractive indices n_H and n_L.

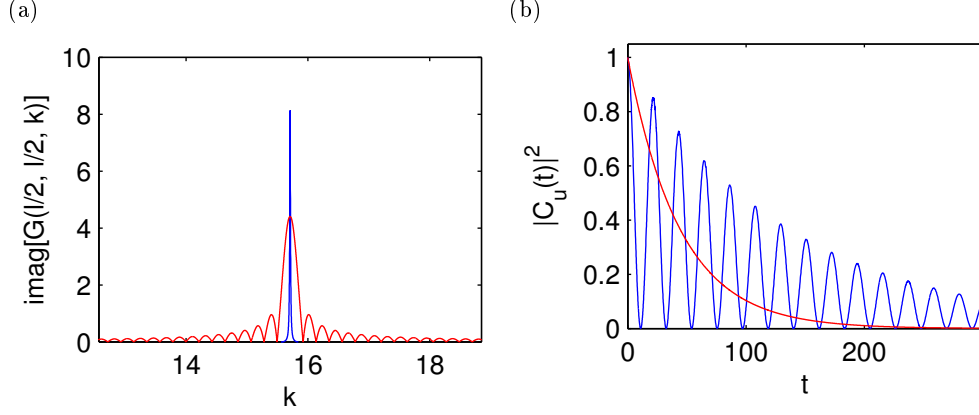(a)   (b)

Figure 4.13.: The same system as in Fig. 4.11 is considered with a different dipole moment $\mu = 0.038$. In (a) G^R (blue) and the weighting function $|\frac{\sin((k-k_A)/(3\Gamma_0))}{k-k_A}| * 0.3$ (red) are displayed. This system is still attributed to the single-mode coupling regime. In (b) the Markov decay (red) suggests for certain time ranges a lower occupation probability than the true value for $|C_u|^2$ (blue).

Further increasing the dipole moment leads us to the last example we want to present in the single mode coupling regime (Fig. 4.13). In this example Rabi oscillations are still visible, but now for the first time the decay is not enhanced for all times t. This scenario occurs because, as discussed earlier, the Markov decay rate increases for increasing dipole moments. In this example the reflection probability, calculated in Eq. (4.8) for two chosen times, exceeds the Markov decay (Red curve in Fig. 4.12(b)). This is why there are ranges of t where the occupation probability of the upper state is higher than the Markov decay suggests.

This setup represents the limit of the single coupling regime. Of course the dipole moment selected in Fig. 4.13 is not the absolute highest value with whom single mode coupling can still be achieved, especially as this limit is a matter of definition. But the qualitative characteristics do not change anymore until the next regime is reached. That is the few-mode coupling regime, which we will discuss in the following section.

4.2.2. Few-mode coupling

In this section we are going to present the few-mode coupling regime. As it is not possible to define clearly when the emitter couples to only one or more modes we will discuss the crossover cases between the obvious single-mode and the obvious multi-
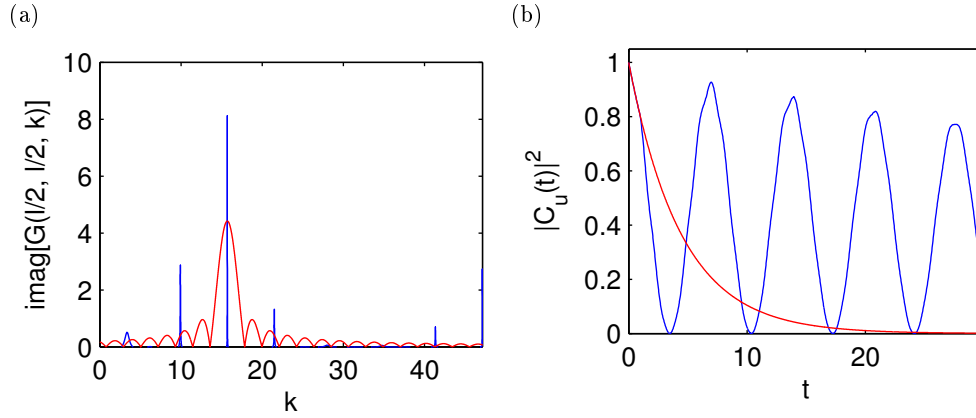
(a)

(b)

Figure 4.14.: The same system as in Fig. 4.11 is considered with a different dipole moment $\mu = 0.12$. In (a) G^R (blue) and the weighting function $|\frac{\sin((k-k_A)/(3\Gamma_0))}{k-k_A}| * 3$ (red) are displayed. In the few-mode coupling regime the resonance at $k_A = 5\pi$ is still the main contributor but the adjacent modes can not be neglected anymore. In (b) $|C_u|^2$ (blue) equates the Markov decay (red) up to the return time $t_r = 1$. For larger times damped oscillations appear.

mode coupling here. The comparison of the weighting function with the Green's function in the two examples presented in this section are shown in Figs. 4.13(a) and 4.14(a). We see that the main contribution still comes from the resonance coinciding with the transition frequency. But the adjacent modes are definitely not negligible anymore.

In these systems the return time t_r plays an important role as well. Like in the single-mode coupling systems (section 4.2.1) the return time is always $t_r = c\,n\,l = 1.0$, in the geometry chosen here. Up to that time the TLS has no information about the size of the cavity. That is why C_u shows exactly the Markov decay up to the return time t_r (Figs. 4.13(b) and 4.14(b)). In this time range the decay looks exactly the same as in the vacuum, i.e., in an infinitely big slab with constant refractive index $n_L = 1.0$. Only as soon as the TLS has information about the cavity dimensions $|C_u|^2$ deviates from the exponential Markov decay. The upper state occupation probability starts to oscillate at $t = t_r$. However, in this regime the oscillations are distorted, which occurs due to the additional resonances the TLS couples with. The distortion of the oscillations gets gradually stronger for larger dipole moments, which can be observed when comparing the upper state occupation probability in Fig. 4.13(b) with Fig. 4.14(b).

We have already seen on the basis of the examples featuring the dielectric slab
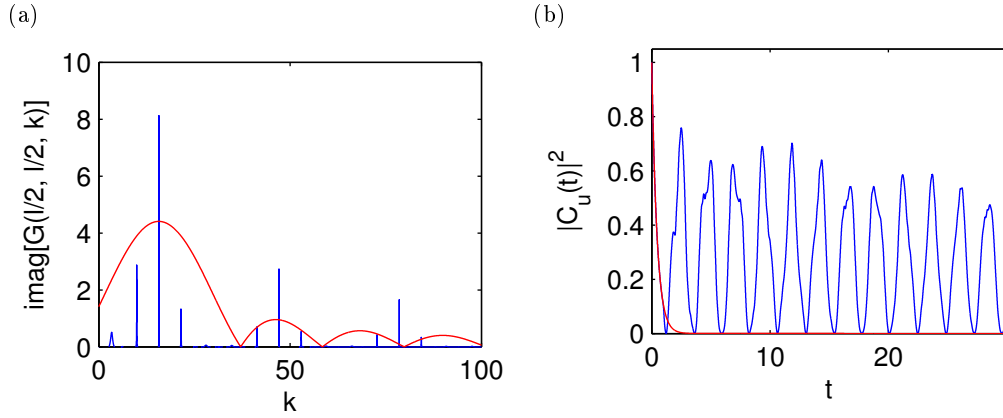
(a)   (b)

Figure 4.15.: The plots shown here, illustrate the same as in Fig. 4.14, but with a dipole
             moment $\mu = 0.38$ and a scaling factor of 30 in the weighting function
             (red curve in (a)). The larger dipole moment causes a stronger interaction
             with the modes in the vicinity of k_A in (a) and a smaller time scale of the
             dynamics in (b).

with and without $\lambda/4$-layers, that the time scale of the dynamics decreases for
increasing dipole moment. Not surprisingly this trend continues in the few-mode
coupling regime. The examples in Figs. 4.14 and 4.15 point out the importance of
the return time t_r. Further increasing the dipole moment will eventually cause the
initial Markov decay to take place on a time scale smaller than t_r. This limit will
be the topic of the next section.

Before we consider the multi-mode coupling regime we show the characteristics
of $|C_u|^2$ in case the emitter is not in tune with a cavity resonance. Similar to
the examples in the single-mode coupling (section 4.2.1) the transition frequency
is now with $k_A = 4\pi$ chosen right between the resonances 3π and 5π. Other than
in the regime of single-mode coupling the upper state occupation probability does
not stay at $|C_u|^2 = 1$. Because the weighting function is now wide enough to
span over the adjacent modes, the emitter always couples at least weakly to the
closest resonances, even for the maximal detuning displayed in Fig. 4.16. Instead
we observe for the probability $|C_u|^2$ oscillations with an offset (Figs. 4.15(a) and
(b)). The offset occurs, because due to the weakened coupling, the emission rate is
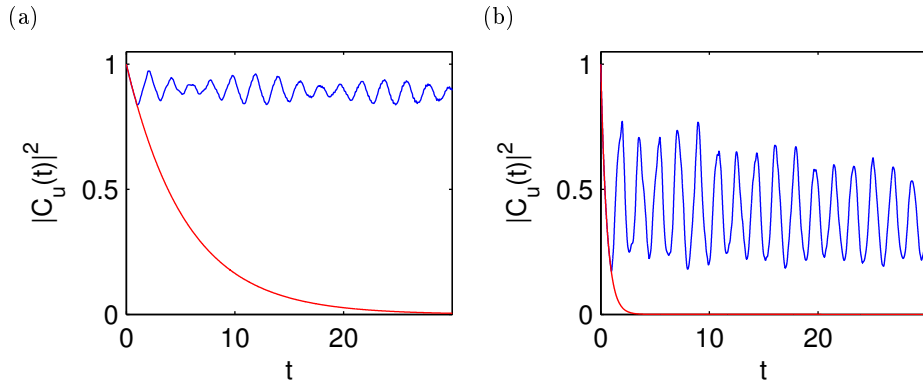smaller compared to Figs. 4.13(b) and 4.14(b).

Figure 4.16.: Behavior of $|C_u|^2$ when k_A is not in tune with a resonance. Except for the transition frequency $k_A = 4\pi$ (a) was calculated using the same system as in Fig. 4.14 ($\mu = 0.12$) and (b) was calculated using the same system as in Fig. 4.15 ($\mu = 0.38$). As the interaction with the resonance at $k = 5\pi$ is weakened, the amplitude of the oscillations is smaller.

4.2.3. Multi-mode coupling

Finally we are going to discuss the multi-mode coupling regime. The dipole moment is considerably large now, causing the weighting function to span over many resonances (Fig. 4.16(a)). Due to the wide peak of the weighting function there is hardly a difference between the contribution of the central mode and the adjacent mode. Furthermore the coupling between the TLS and the cavity resonances is very strong now, so the photon is emitted very fast. Compared to the return time $t_r = 1.0$, the emitter decays almost instantly. The characteristics of the upper state probability (Fig. 4.16(b)) can be explained in a quasi-classical picture: The light pulse is emitted from the TLS at $t = 0$, after which the TLS is in the ground state until the reflected pulse comes back and is reabsorbed at $t = t_r = 1.0$. This procedure repeats itself, with decaying reabsorption probability due to the loss during the reflection. The second pulse is also visible in Fig. 4.16(b). Note that the peaks of the pulses do not exactly occur at integer multiples of the return time. This is because the $\lambda/4$-layers have a finite size and the peak of the light pulse is therefore not reflected right at the first refractive index transition. Instead the peaks have two local maxima which correspond to the refractive index transition of the $\lambda/4$ layers.

The size of the peaks in $|C_u|^2$ is also not as easy to calculate, as in the single-mode coupling regime because the reflection depends on the wavelength λ. There are many modes contributing so one would have to take the average reflection in the

(a)   (b)
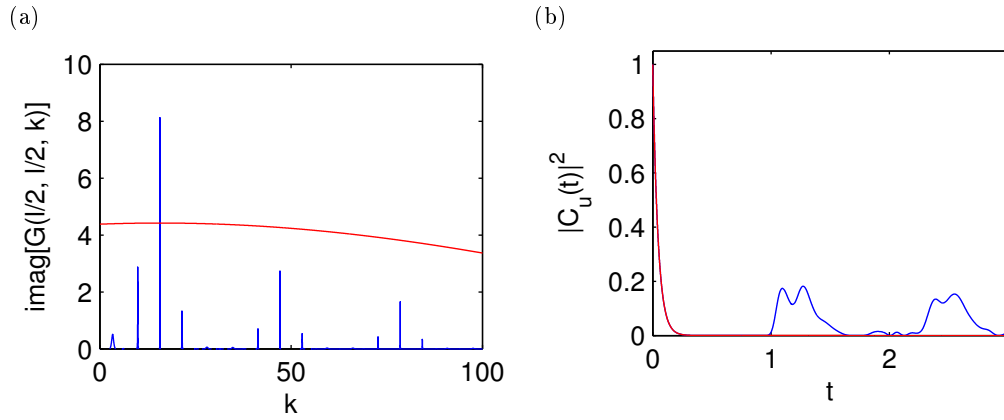

Figure 4.17.: The same system as in Fig. 4.11 is considered with a different dipole
moment $\mu = 1.2$. In (a) G^R (blue) and the weighting function
$|\frac{\sin((k-k_A)/(3\Gamma_0))}{k-k_A}| * 300$ (red) are displayed. The weighting function spans
over many cavity modes. In the multi-mode coupling regime, the behavior
of $|C_u|^2$ (blue curve in (b)) can be explained quasi-classically: the photon
bounces back and forth in the cavity and can be reabsorbed every time it
passes the emitter.

considered wavelength range to get the correct peak height. But when comparing
Fig. 4.16(b) with the multi-mode result for the dielectric slab Fig. 4.6(b) one notices
that the peak height is roughly the same. The peak shapes differ because of the
additional refractive index transitions after the initial scattering in the case of the
$\lambda/4$-layers. This demonstrates that the $\lambda/4$-layers do not significantly change the
reflection probability for frequencies other than the one they are tuned to. With
this example we conclude the presentation of our results.

Chapter 5.

Summary and Outlook

In this thesis we investigated the emission characteristics of an excited two-level system (TLS) placed in a one-dimensional cavity. We used a fully quantum approach [10] to derive the basic equations, which were later solved numerically.

We presented results for a TLS placed in a dielectric slab with and without $\lambda/4$-layers to its left and right. The behavior of the TLS depends heavily on how strong it couples with the cavity modes. This coupling strength is mostly controlled by the coupling constant, i.e., the dipole moment μ. Depending on the order of magnitude of the dipole moment, we classified three different regimes: single-mode, few-mode and multi-mode coupling. As the different names suggest, the TLS interacts in these three different regimes with either one, several or many modes of the cavity. For an increasing amount of modes coupling to the TLS the time scale of the decay to the ground state does not only get smaller, but its qualitative behavior changes as well.

In the single-mode coupling regime we observed well known phenomena such as the Markov decay, enhanced Markov decay due to the Purcell effect, and Rabi oscillations. While the Markov decay is easy to observe in any cavity, certain requirements must be met by the dipole moment and the cavity in order to observe Rabi oscillations. The coupling must have a considerable strength while staying in the single mode coupling regime. Furthermore the mode with which the TLS couples, needs to have a long dwell time in the cavity, which was achieved using $\lambda/4$-layers. In case the TLS is not tuned close enough to a cavity resonance, it will stay in the excited state and not emit the photon, as there are no available modes.

The few-mode coupling regime provides a very interesting insight into the transition from single-mode to multi-mode coupling. In these systems the central mode remains the major contributor, but the adjacent modes are no longer negligible. This can be shown by detuning the TLS transition right between two resonances, as the TLS will not stay in the excited state anymore, because it weakly couples to the modes in the proximity. For few-mode coupling the return time becomes important. This time measures how long takes for the photon to travel from the TLS to the closest possible point of scattering and back to the TLS. At this time scale the emitter receives information about the dimension of the cavity and deviates from the Markov decay.

With the numerical tools developed in this thesis we are also capable of performing calculations in the multi-mode coupling regime where conventional approaches tend to fail. In this regime we obtain results for the upper state occupation probability of the TLS which can be understood in a quasi-classical picture. The photon is emitted almost instantly and bounces back and forth in the cavity. Each time the photon passes the TLS, a raised reabsorption probability is observed.

The obvious next step in our calculations would be to extend them to two- or even three-dimensional systems. The greatest challenge in doing so is the numerically very demanding calculation of the reflection Green's function G^R for a large range of k-vectors. Once this is achieved, the only other equation modified by the additional dimension(s) is the Green's function describing the propagation in the medium G^M. All the following equations remain unmodified. The characteristics of G^M, or G in general, might also require a different treatment of the diverging integral in the kernel integral Eq. (3.22), as the Green's functions no longer decreases for increasing frequencies.

In this thesis we achieved multi-mode coupling by increasing the dipole moment to an according value. In the real world we suspect the easier way would be to increase the local density of states (LDOS). There are already experimental realizations to measure strong coupling phenomena in the single-mode coupling regime, such as Rabi oscillations. If the LDOS is increased in such a system, for example by a larger cavity or using two- or three-dimensional systems, the limit of multi-mode coupling is reachable. As our numerical tools are applicable for arbitrary cavities, they could provide a powerful basis to simulate almost any experimental setup.

Acknowledgements

First and foremost I would like to thank my advisor Prof. Stefan Rotter who spent uncountable hours — on weekdays, weekends and holidays, alike — to discuss any problem or question I had, not only during this thesis, but also during the previous projects in which I had the pleasure of benefitting from his guidance. Through his expertise in physics and creative approach to problem solving, he always provided me with precious hints to guide me in the right direction. In addition to his invaluable help in physics I also want to thank him for his support in making it possible for me to stay one month in Princeton, New Jersey and work at Princeton University with Prof. Hakan Türeci, who inspired us to concentrate our research on this topic. Without Stefan's financial and organizational support this would not have been possible.

I also want to thank my office mate Matthias Liertzer. His broad knowledge, competence, and experience in numerical programming and computer problems as a whole saved me many hours of frustrating trial and error. This was in addition to his support in many physics related questions. As we shared an office throughout the whole duration of my thesis, he was often the first person with whom I discussed my questions.

During my stay at the Princeton university I was fortunate enough to meet Prof. Hakan Türeci. In the short amount of time I had in Princeton we had some very instructional talks. His experience and insight in the field of quantum optics and physics in general was of great help with the fundamental questions I encountered during my research. Staying in his group was a very enlightening experience and gave me an inspiring impression of the different aspects of working in the scientific community. Among the other people I met in Princeton, I especially want to thank Bojan Skerlak for spending a lot of time with me not only at the office but also during our free time.

Besides Matthias I also want to thank all the other people with whom I shared an office during the course of my thesis. Adrian Girschik, Thomas Hisch, Phillip Ambichl and Konstantinos Makris all contributed to a comfortable and open working environment. I could not have wished for a better atmosphere in which to develop my ideas and complete my research.

Last, but not least, I want to thank my family and my girlfriend Coralie. My family offered me the unconditional and crucial moral and financial support that I needed during the past five years. They always made it clear that getting the

maximum out of my studies was the most important thing. Coralie was the most important person in my life over the past three years and therefore influenced every decision I made and my performance in the most positive way, for which I could not be more thankful.

Appendix A.

Hamiltonian in Dipole and Rotating-Wave Approximation

We start with the Hamiltonian, Eq. (2.14), describing an atom in the electric field. The atom is approximated by a two-level system (TLS) and the dipole approximation (DA) and the rotating-wave approximation (RWA) are applied to obtain the Hamiltonian, Eq. (2.19), used to describe the behavior of an emitter in an optical cavity. Multiplying out Eq. (2.16) and neglecting the small $\hat{\mathbf{A}}^2$ term we can split up the kinetic energy, Eq. (2.16), and the Coulomb energy, Eq. (2.17), in two parts describing the energy of the atom and the atom-field interaction

$$\hat{H}_{\text{Atom}} = \sum_\alpha \frac{\hat{\mathbf{p}}_\alpha^2}{2m_\alpha} + \frac{1}{2} \int \mathrm{d}^3\mathbf{r} \hat{\rho}_A(\mathbf{r}) \hat{\phi}_A(\mathbf{r}), \tag{A.1}$$

$$\hat{H}_{\text{Atom-field}} = \sum_\alpha \frac{q_\alpha}{2m_\alpha} \left\{ \hat{\mathbf{p}}_\alpha, \hat{\mathbf{A}}_\alpha(\hat{\mathbf{r}}_\alpha) \right\} + \int \mathrm{d}^3\mathbf{r} \hat{\rho}_A(\mathbf{r}) \hat{\phi}(\mathbf{r}). \tag{A.2}$$

First we restrict the atom to a simple two-level system. Hence Eq. (A.1) becomes

$$\hat{H}_{\text{Atom}} = \hbar\omega_u |u\rangle\langle u| + \hbar\omega_l |l\rangle\langle l|. \tag{A.3}$$

Putting zero energy centered between the upper excited and the lower ground state, so that $\omega_u = -\omega_l = \omega_A/2$ and using vector notation for the upper state $|u\rangle$ and the lower state $|l\rangle$ we get

$$\begin{pmatrix} 1 \\ 0 \end{pmatrix} * \begin{pmatrix} 1 & 0 \end{pmatrix} - \begin{pmatrix} 0 \\ 1 \end{pmatrix} * \begin{pmatrix} 0 & 1 \end{pmatrix} = \begin{pmatrix} 1 & 0 \\ 0 & -1 \end{pmatrix} = \hat{\sigma}_z. \tag{A.4}$$

So for the atom energy we get the well known Hamiltonian

$$\hat{H}_{\text{Atom}} = \frac{1}{2} \hbar\omega_A \hat{\sigma}_z. \tag{A.5}$$

In the next step we look at the Coulomb term of Eq. (A.2). For the charge density we insert an electric dipole,

$$\hat{\rho}_A(\mathbf{r}) = q\,\delta\left(\mathbf{r} - \hat{\mathbf{r}}_A + \frac{\hat{\mathbf{d}}}{2}\right) - q\,\delta\left(\mathbf{r} - \hat{\mathbf{r}}_A + \frac{\hat{\mathbf{d}}}{2}\right), \tag{A.6}$$

and make the dipole approximation

$$
\int d^3\mathbf{r}\hat{\rho}_A(\mathbf{r})\hat{\phi}(\mathbf{r}) = q\left[\hat{\phi}\left(\hat{\mathbf{r}}_A + \frac{\hat{\mathbf{d}}}{2}\right) - \hat{\phi}\left(\hat{\mathbf{r}}_A - \frac{\hat{\mathbf{d}}}{2}\right)\right] \overset{\text{DA}}{\approx} q\left[\hat{\phi}\left(\mathbf{r}_A\right) + \frac{\hat{\mathbf{d}}}{2}\cdot\nabla\hat{\phi}(\mathbf{r}_A) - \right.
$$

$$
\left. -\hat{\phi}\left(\mathbf{r}_A\right) + \frac{\hat{\mathbf{d}}}{2}\cdot\nabla\hat{\phi}(\mathbf{r}_0)\right] = q\hat{\mathbf{d}}\cdot\nabla\hat{\phi}(\mathbf{r}_A) = -\hat{\boldsymbol{\mu}}\cdot\nabla\hat{\phi}(\mathbf{r}_A). \qquad \text{(A.7)}
$$

Now we rewrite the dipole operator

$$
\hat{\boldsymbol{\mu}} = q\,\hat{\mathbf{d}} = q\left(|u\rangle\langle u| + |l\rangle\langle l|\right)\hat{\mathbf{d}}\left(|u\rangle\langle u| + |l\rangle\langle l|\right) = q\left(|u\rangle\langle u|\hat{\mathbf{d}}|u\rangle\langle u| + \right.
$$

$$
\left. + |l\rangle\langle l|\hat{\mathbf{d}}|l\rangle\langle l| + |u\rangle\langle u|\hat{\mathbf{d}}|l\rangle\langle l| + |l\rangle\langle l|\hat{\mathbf{d}}|u\rangle\langle u|\right) =
$$

$$
= \underbrace{q\langle u|\hat{\mathbf{d}}|l\rangle}_{\boldsymbol{\mu}}\underbrace{|u\rangle\langle l|}_{\hat{\sigma}_+} + \underbrace{q\langle l|\hat{\mathbf{d}}|u\rangle}_{\boldsymbol{\mu}}\underbrace{|l\rangle\langle u|}_{\hat{\sigma}_-}, \qquad \text{(A.8)}
$$

where we made use of the fact that $\hat{\mathbf{d}}$ has negative parity and therefore $\langle u|\hat{\mathbf{d}}|u\rangle = \langle l|\hat{\mathbf{d}}|l\rangle = 0$. Splitting up the potential in its positive and negative frequency components yields

$$
\int d^3\mathbf{r}\hat{\rho}_A(\mathbf{r})\hat{\phi}(\mathbf{r}) = \boldsymbol{\mu}\left(\hat{\sigma}_+ + \hat{\sigma}_-\right)\left(\int_{-\infty}^0 d\omega\,\nabla\hat{\phi}(\mathbf{r}_A,\omega) + \text{H.c.}\right) =
$$

$$
\overset{\text{RWA}}{\approx} \boldsymbol{\mu}\hat{\sigma}_+ \int_{-\infty}^0 d\omega\,\nabla\hat{\phi}(\mathbf{r}_A,\omega) + \text{H.c.} \qquad \text{(A.9)}
$$

We still have to take care of the first term in (A.2). In the Heisenberg-picture the time evolution of an operator can be calculated using

$$
\frac{d}{dt}\hat{A}_H(t) = \frac{\partial}{\partial t}\hat{A}_H(t) + \frac{1}{i\hbar}\left[\hat{A}_H(t), \hat{H}_H(t)\right]. \qquad \text{(A.10)}
$$

Applying this relation on the (Schrödinger-)space and momentum operators yields

$$
\hat{\mathbf{p}}_\alpha \approx \frac{m_\alpha}{i\hbar}\left[\hat{\mathbf{r}}_\alpha, \hat{H}_{\text{Atom}}\right]. \qquad \text{(A.11)}
$$

Now we can use this relation

$$
\sum_\alpha \frac{q_\alpha}{2m_\alpha}\left\{\hat{\mathbf{p}}_\alpha, \hat{\mathbf{A}}(\hat{\mathbf{r}}_\alpha)\right\} = \sum_\alpha \frac{q_\alpha}{2m_\alpha}\left\{\frac{m_\alpha\omega_A}{2i}\left[\hat{\mathbf{r}}_\alpha, \hat{\sigma}_z\right], \hat{\mathbf{A}}(\hat{\mathbf{r}}_\alpha)\right\} =
$$

$$
= \sum_\alpha \frac{q_\alpha\omega_A}{4i}\left\{\left[\hat{\mathbf{r}}_\alpha, \hat{\sigma}_z\right], \hat{\mathbf{A}}(\hat{\mathbf{r}}_\alpha)\right\} \overset{\text{DA}}{\approx} \frac{q\omega_A}{4i}\left\{\left[\hat{\mathbf{d}}, \hat{\sigma}_z\right], \hat{\mathbf{A}}(\mathbf{r}_A)\right\}, \qquad \text{(A.12)}
$$

where

$$q \left[\hat{\mathbf{d}}, \hat{\sigma}_z\right] = \boldsymbol{\mu} \left[\hat{\sigma}_+, \hat{\sigma}_z\right] + \boldsymbol{\mu} \left[\hat{\sigma}_-, \hat{\sigma}_z\right] = -2\boldsymbol{\mu}\hat{\sigma}_- + 2\boldsymbol{\mu}\hat{\sigma}_+. \tag{A.13}$$

We also rewrite the vector potential as

$$\omega_A \hat{\mathbf{A}}(\mathbf{r}_A) \overset{\text{RWA}}{\approx} \int_{-\infty}^{\infty} \mathrm{d}\omega\, \omega \hat{\mathbf{A}}(\mathbf{r}, \omega) = -i \int_{-\infty}^{\infty} \mathrm{d}\omega\, i\omega \hat{\mathbf{A}}(\mathbf{r}, \omega) =$$
$$= -i \left(\int_{-\infty}^{0} \mathrm{d}\omega\, i\omega \hat{\mathbf{A}}(\mathbf{r}, \omega) - \text{H.c.} \right). \tag{A.14}$$

So the first term in (A.2) becomes

$$-\boldsymbol{\mu} \left(\hat{\sigma}_+ - \hat{\sigma}_-\right) \left(\int_{-\infty}^{0} \mathrm{d}\omega\, i\omega \hat{\mathbf{A}}(\mathbf{r}, \omega) - \text{H.c.} \right) \overset{\text{RWA}}{\approx} -\boldsymbol{\mu}\hat{\sigma}_+ \int_{-\infty}^{0} \mathrm{d}\omega\, i\omega \hat{\mathbf{A}}(\mathbf{r}, \omega) - \text{H.c.}$$
$$\tag{A.15}$$

In classical electrodynamics the electric field can be written in terms of potentials

$$\mathbf{E}(\mathbf{r}, t) = -\nabla\varphi(\mathbf{r}, t) - \frac{\partial}{\partial t}\mathbf{A}(\mathbf{r}, t), \tag{A.16}$$

which becomes in frequency domain

$$\mathbf{E}(\mathbf{r}, \omega) = -\nabla\varphi(\mathbf{r}, \omega) + i\omega \mathbf{A}(\mathbf{r}, \omega). \tag{A.17}$$

We adopt this results for the time-independent Schrödinger operators. Hence the final result for the Atom-field Hamiltonian, Eq. (A.2), is

$$\hat{H}_{\text{Atom−field}} = -\boldsymbol{\mu}\hat{\sigma}_+ \int_{-\infty}^{0} \mathrm{d}\omega\, \mathbf{E}(\mathbf{r}_A, \omega) - \text{H.c.} = -\hat{\sigma}_+ \mathbf{E}^{(+)}(\mathbf{r}_A) \cdot \boldsymbol{\mu} - \text{H.c.}, \tag{A.18}$$

which leads to the final result Eq. (2.19).

Appendix B.

Calculating C_u and C_{li}

Starting with the Hamiltonian, Eq. (2.19), the electric field operator, Eq. (2.13), and the ansatz for the wave function ψ, Eq. (2.20), we show a more detailed calculation of the basic Eqs. (2.21) and (2.22), describing the upper state amplitude of the TLS. We start by applying each term of the Hamiltonian on the wave function. We get a term for the field Hamiltonian

$$\hat{H}_{\text{field}}|\psi(t)\rangle = \int \mathrm{d}^3\mathbf{r} \int_0^\infty \mathrm{d}\omega \, C_{li}(\mathbf{r}, \omega, t) e^{-i(\omega - \frac{\omega_A}{2})} \hbar\omega \, |l\rangle|1_i(\mathbf{r}, \omega)\rangle, \qquad (\text{B.1})$$

as well as for the atom Hamiltonian

$$\hat{H}_{\text{Atom}}|\psi(t)\rangle = \frac{1}{2}\hbar\omega_A \, C_u(t) e^{-\frac{\omega_A}{2}t}|u\rangle|0\rangle -$$
$$-\frac{1}{2}\hbar\omega_A \int \mathrm{d}^3\mathbf{r} \int_0^\infty \mathrm{d}\omega \, C_{li}(\mathbf{r}, \omega, t) e^{-i(\omega - \frac{\omega_A}{2})t}|l\rangle|1_i(\mathbf{r}, \omega)\rangle, \qquad (\text{B.2})$$

and for the atom-field interaction Hamiltonian

$$\hat{H}_{\text{Atom-field}}|\psi(t)\rangle =$$
$$-\int \mathrm{d}^3\mathbf{r} \int_0^\infty \mathrm{d}\omega \, i\frac{\omega^2}{c^2}\sqrt{\frac{\hbar}{\pi\epsilon_0}}\sqrt{\mathrm{Im}\,\epsilon(\mathbf{r}, \omega)} G(\mathbf{r_A}, \mathbf{r}, \omega)\mu \, C_{li}(\mathbf{r}, \omega, t) e^{-i(\omega - \frac{\omega_A}{2})t}|u\rangle|0\rangle +$$
$$+\int \mathrm{d}^3\mathbf{r} \int_0^\infty \mathrm{d}\omega \, i\frac{\omega^2}{c^2}\sqrt{\frac{\hbar}{\pi\epsilon_0}}\sqrt{\mathrm{Im}\,\epsilon(\mathbf{r}, \omega)} G^*(\mathbf{r_A}, \mathbf{r}, \omega)\mu \, C_u(t) e^{-i\frac{\omega_A}{2}t}|l\rangle|1_i(\mathbf{r}, \omega)\rangle.$$
$$(\text{B.3})$$

To employ the Schrödinger equation, we also need to calculate the time-derivative of the wave function $|\psi\rangle$

$$i\hbar\frac{\partial}{\partial t}|\psi(t)\rangle = \frac{1}{2}\hbar\omega_A \, C_u(t) e^{-\frac{\omega_A}{2}t}|u\rangle|0\rangle +$$
$$+\int \mathrm{d}^3\mathbf{r} \int_0^\infty \mathrm{d}\omega \left(\hbar\omega - \frac{1}{2}\hbar\omega_A\right) C_{li}(\mathbf{r}, \omega, t) e^{-i(\omega - \frac{\omega_A}{2})t}|l\rangle|1_i(\mathbf{r}, \omega)\rangle -$$
$$\dot{C}_u(t) e^{-i\omega_A t/2}|u\rangle|0\rangle + \int \mathrm{d}^3\mathbf{r} \int_0^\infty \mathrm{d}\omega \, \dot{C}_{li}(\mathbf{r}, \omega, t) e^{-i(\omega - \omega_A/2)t}|l\rangle|\{1_i(\mathbf{r}, \omega)\}\rangle.$$
$$(\text{B.4})$$

Equations (B.1), (B.2), (B.3) and (B.4) are plugged into the Schrödinger equation. Terms that cancel each other are indicated by the respective color. Since $|u\rangle|0\rangle$ and $|l\rangle|1_i(\mathbf{r},\omega)\rangle$ are orthogonal to each other we can compare their coefficients. For the upper state amplitude we get

$$\dot{C}_u(t) = -\frac{\mu}{\sqrt{\pi\epsilon_0\hbar}} \int_0^\infty \mathrm{d}\omega \frac{\omega^2}{c^2} \int \mathrm{d}^3\mathbf{r} \left[\sqrt{\epsilon_I(\mathbf{r},\omega)} G(\mathbf{r}_A,\mathbf{r},\omega) C_{li}(\mathbf{r},\omega,t) e^{-i(\omega-\omega_A)t} \right],$$
(B.5)

and the lower state amplitude is

$$\dot{C}_{li}(\mathbf{r},\omega,t) = -\frac{\mu}{\sqrt{\pi\epsilon_0\hbar}} \frac{\omega^2}{c^2} \sqrt{\epsilon_I(\mathbf{r},\omega)} G^*(\mathbf{r}_A,\mathbf{r},\omega) C_{li}(\mathbf{r},\omega,t) e^{i(\omega-\omega_A)t}.$$
(B.6)

Now we integrate Eq. (B.6) (with the initial condition $C_{li}(\mathbf{r},\omega,0) = 0$) over time

$$C_{li}(\mathbf{r},\omega,t) = -\frac{\mu}{\sqrt{\pi\epsilon_0\hbar}} \frac{\omega^2}{c^2} \sqrt{\epsilon_I(\mathbf{r},\omega)} G^*(\mathbf{r}_A,\mathbf{r},\omega) \int_0^t C_{li}(\mathbf{r},\omega,t') e^{i(\omega-\omega_A)t'} \, \mathrm{d}t', \quad \text{(B.7)}$$

and insert it into Eq. (B.5)

$$\dot{C}_u(t) = -\frac{\mu^2}{\pi\epsilon_0\hbar} \left[\int_0^\infty \mathrm{d}\omega \frac{\omega^2}{c^2} e^{-i(\omega-\omega_A)t} \left(\int_0^t C_u(t') e^{i(\omega-\omega_A)t'} \, \mathrm{d}t' \right) \right.$$
$$\left. \left(\int \mathrm{d}^3\mathbf{r} \frac{\omega^2}{c^2} [\mathrm{Im}\,\epsilon(\mathbf{r},\omega)] G(\mathbf{r}_A,\mathbf{r},\omega) G^*(\mathbf{r}_A,\mathbf{r},\omega) \right) \right].$$
(B.8)

Equation (B.8) can be simplified using the relation [10]

$$\mathrm{Im}\,G(\mathbf{r},\mathbf{r}',\omega) = \int \mathrm{d}^3\mathbf{s} \frac{\omega^2}{c^2} [\mathrm{Im}\,\epsilon(\mathbf{s},\omega)] G(\mathbf{r},\mathbf{s},w) G^*(\mathbf{r}',\mathbf{s},w),$$
(B.9)

yielding the final result

$$\dot{C}_u(t) = -\frac{\mu^2}{\pi\epsilon_0\hbar} \int_0^\infty \mathrm{d}\omega \frac{\omega^2}{c^2} \left(\int_0^t C_u(t') e^{i(\omega-\omega_A)(t-t')} \, \mathrm{d}t' \right) \mathrm{Im}\,G(\mathbf{r}_A,\mathbf{r}_A,\omega), \quad \text{(B.10)}$$

which can easily be rewritten as Eqs. (2.21) and (2.22).

Appendix C.

Regularization of the 1D Gauss function

As discussed earlier the emitter is no a perfect point like source, therefore we replace the Green's function by its average over a small area. We use the vacuum Green's function $G(x_1, x_2, k)$ and calculate the average for both spatial dependencies in the interval $[a, b]$,

$$G^{\text{reg}}(x_A, x_A, k) = \frac{1}{(a-b)^2} \int_a^b \int_a^b \frac{i}{2k} e^{ik|x_1 - x_2|} \, \mathrm{d}x_1 \, \mathrm{d}x_2, \tag{C.1}$$

which can be solved analytically. The first integral gives

$$\int_a^b e^{ik|x_1 - x_2|} \, \mathrm{d}x_1 = \int_a^{x_2} e^{ik(x_2 - x_1)} \, \mathrm{d}x_1 + \int_{x_2}^b e^{ik(x_1 - x_2)} \, \mathrm{d}x_1 =$$

$$= \frac{-1}{ik} \left(1 - e^{ik(x_2 - a)} \right) + \frac{1}{ik} \left(e^{ik(b-x_2)-1} \right)$$

$$= \frac{1}{ik} \left(e^{ik(x_2 - a)} + e^{ik(b-x_2)} + 2 \right). \tag{C.2}$$

For the second integral we have

$$\int_a^b \frac{1}{ik} \left(e^{ik(x_2 - a)} + e^{ik(b-x_2)} + 2 \right) \, \mathrm{d}x_2 = \frac{1}{ik} \left[\frac{1}{ik} \left(e^{ik(b-a)} - 1 \right) \right.$$

$$\frac{-1}{ik} \left(1 - e^{ik(b-a)} \right) - 2(b-a) \bigg] = \frac{2}{k^2} \left[1 - e^{ik(b-a)} + ik(b-a) \right]. \tag{C.3}$$

Rewriting this we recognize the vacuum Green's function evaluated at $x_1 = x_2$

$$G^{\text{reg}}(x_A, x_A, k) = \frac{i}{2k} * \frac{2}{k^2(b-a)^2} \left[1 - e^{ik(b-a)} + ik(b-a) \right]$$

$$= G(x_A, x_A, k) * \frac{2}{k^2(b-a)^2} \left[1 - e^{ik(b-a)} + ik(b-a) \right]. \tag{C.4}$$

To calculate the kernel integral, Eq. (2.24), we need the imaginary part of the Green's function

$$\text{Im} \, G^{\text{reg}}(x_A, x_A, k) = \text{Im} \, G(x_A, x_A, k) \, \frac{2}{k^2(b-a)^2} \left[1 - \cos \left(k(b-a) \right) \right], \tag{C.5}$$

which yields the regularized Green's function

$$\text{Im}\,G^{\text{reg}}(x_A, x_A, k) = \text{Im}\,G(x_A, x_A, k)\,\frac{\sin^2\left(\frac{k}{2}(b-a)\right)}{\left(\frac{k}{2}(b-a)\right)^2}. \qquad (C.6)$$

The regularized Green's function G^{reg} contains an additional factor Eq. (3.20), compared to the Green's function G evaluated at the position of the emitter x_A.

Appendix D.

Adaptive Solution of the Volterra Integral Equation

We present here the principles of the algorithm used to numerically solve the Volterra Integral equation (2.23) [22]

$$f(t) = \int_0^t k(t-\tau)f(\tau)\,\mathrm{d}\tau + 1. \tag{D.1}$$

An adaptive step-width is used for the time t, which is chosen based on the user-specified error tolerance. We discretize the variable t according to figure D.1, using the following nomenclature:

$$t_n = \sum_{m=0}^{n} h_m\,, \quad k(t_n - t_m) = k_{n,m}\,, \quad f(t_n) = f_n. \tag{D.2}$$

Splitting up every step in a separate integral yields

$$f_n = \sum_{m=0}^{n-1} \int_{t_m}^{t_{m+1}} k(t_n - \tau)f(\tau)\,\mathrm{d}\tau + 1. \tag{D.3}$$
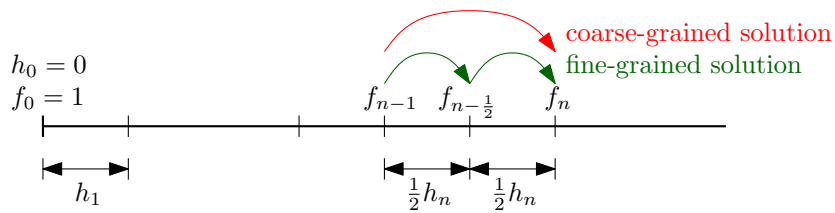

Figure D.1.: For the numerical solution of the Volterra integral an algorithm with adaptive step-width was implemented. The step-width was chosen by calculating the relative error between the coarse-grained solution and the fine-grained solution

Applying the trapezoidal rule (and $h_0 = 0$) we get

$$
\begin{aligned}
f_n &= \sum_{m=0}^{n-1} \frac{1}{2} h_{m+1} \left(k_{n,m} f_m + k_{n,m+1} f_{m+1} \right) + 1 \\
&= \sum_{m=0}^{n-1} \frac{1}{2} h_{m+1} k_{n,m} f_m + \sum_{m=1}^{n} \frac{1}{2} h_m k_{n,m} f_m + 1 \\
&= \sum_{m_0}^{n-1} \frac{1}{2} \left(h_m + h_{m+1} \right) k_{n,m} f_m + \frac{1}{2} h_n k_{n,n} f_n + 1.
\end{aligned}
\tag{D.4}
$$

Hence f_n can, in general, be calculated using

$$
f_n^{\text{coarse}} = \left(\sum_{m=0}^{n-1} \frac{1}{2} \left(h_m + h_{m+1} \right) k_{n,m} f_m + 1 \right) \left(1 - \frac{1}{2} h_n k_{n,n} \right)^{-1}.
\tag{D.5}
$$

Equation (D.5) is the coarse-grained solution. Next we calculate f_n for a smaller step-width. To obtain the fine-grained solution, the last interval is split into half

$$
\begin{aligned}
f_n^{\text{fine}} = \sum_{m=0}^{n-2} \int_{t_m}^{t_{m+1}} k(t_n - \tau) f(\tau) \, d\tau + \\
+ \int_{t_{n-1}}^{t_{n-\frac{1}{2}}} k(t_n - \tau) f(\tau) \, d\tau + \int_{t_{n-\frac{1}{2}}}^{t_n} k(t_n - \tau) f(\tau) \, d\tau + 1.
\end{aligned}
\tag{D.6}
$$

Using the trapezoidal rule in the same fashion as before

$$
\begin{aligned}
f_n^{\text{fine}} &= \sum_{m=0}^{n-2} \frac{1}{2} h_{m+1} \left(k_{n,m} f_m + k_{n,m+1} f_{m+1} \right) + \frac{1}{4} h_n \left(k_{n,n-1} f_{n-1} + \right. \\
&\quad \left. + k_{n,n-\frac{1}{2}} f_{n-\frac{1}{2}} \right) + \frac{1}{4} h_n \left(k_{n,n-\frac{1}{2}} f_{n-\frac{1}{2}} + k_{n,n} f_n \right) + 1 \\
&= \sum_{m=0}^{n-2} \frac{1}{2} h_{m+1} k_{n,m} f_m + \sum_{m=1}^{n-1} \frac{1}{2} h_m k_{n,m} f_m + \frac{1}{4} h_n k_{n,n-1} f_{n-1} + \\
&\quad + \frac{1}{2} h_n k_{n,n-\frac{1}{2}} f_{n-\frac{1}{2}} + \frac{1}{4} h_n k_{n,n} f_n + 1 \\
&= \sum_{m=0}^{n-2} \frac{1}{2} \left(h_{m+1} + h_m \right) k_{n,m} f_m + \frac{1}{4} \left(h_n + 2 h_{n,n-1} \right) k_{n,n-1} f_{n-1} + \\
&\quad + \frac{1}{2} h_n k_{n,n-\frac{1}{2}} f_{n-\frac{1}{2}} + \frac{1}{4} h_n k_{n,n} f_n + 1,
\end{aligned}
\tag{D.7}
$$

yields for the fine-grained solution

$$f_n^{\text{fine}} = \left(\sum_{m=0}^{n-2} \frac{1}{2} \left(h_{m+1} + h_m \right) k_{n,m} f_m + \frac{1}{4} \left(h_n + 2h_{n,n-1} \right) k_{n,n-1} f_{n-1} + \right.$$
$$\left. + \frac{1}{2} h_n k_{n,n-\frac{1}{2}} f_{n-\frac{1}{2}} + 1 \right) \left(1 - \frac{1}{4} h_n k_{n,n} \right)^{-1}. \tag{D.8}$$

To evaluate the fine-grained solution f_n^{fine} we also need to find an expression for $f_{n,n-\frac{1}{2}}$

$$f_{n-\frac{1}{2}} = \sum_{m=0}^{n-2} \frac{1}{2} h_{m+1} \left(k_{n-\frac{1}{2},m} f_m + k_{n-\frac{1}{2},m+1} f_{m+1} \right) +$$
$$+ \frac{1}{4} h_n \left(k_{n-\frac{1}{2},n-1} f_{n-1} + k_{n-\frac{1}{2},n-\frac{1}{2}} f_{n-\frac{1}{2}} \right) + 1$$
$$= \sum_{m=0}^{n-2} \frac{1}{2} \left(h_m + h_{m+1} \right) k_{n-\frac{1}{2},m} f_m + \frac{1}{4} \left(2h_{n-1} + h_n \right) k_{n-\frac{1}{2},n-1} f_{n-1} +$$
$$+ \frac{1}{4} h_n k_{n-\frac{1}{2},n-\frac{1}{2}} f_{n-\frac{1}{2}} + 1$$
$$\Rightarrow f_{n-\frac{1}{2}} = \left(\sum_{m=0}^{n-2} \frac{1}{2} \left(h_m + h_{m+1} \right) k_{n-\frac{1}{2},m} f_m + \frac{1}{4} \left(2h_{n-1} + \right. \right.$$
$$\left. \left. + h_n \right) k_{n-\frac{1}{2},n-1} f_{n-1} + 1 \right) \left(1 - \frac{1}{4} h_n k_{n-\frac{1}{2},n-\frac{1}{2}} \right)^{-1}. \tag{D.9}$$

The algorithm works as follows:

- Choose an initial step width, an error tolerance and a minimum step width.

- Compute f_n^{fine}, Eqs. (D.8) and (D.9), and f_n^{coarse} , Eq. (D.5), and calculate the relative of those two solutions.

- As long as the error is larger than the specified tolerance and the step width larger than the minimum step width, reduce the step width and repeat the calculation.

- Save the results and repeat until desired maximum time t is reached.

Bibliography

[1] E. M. Purcell, "Spontaneous emission probabilities at radio frequencies," vol. 69, p. 681, 1946.

[2] S. Haroche and D. Kleppner, "Cavity quantum electrodynamics," *Physics Today*, vol. 42, p. 24, 1989.

[3] C. Weisbuch and J. Rarity, *Microcavities and photonic bandgaps: physics and applications.* Springer, 1996.

[4] K. H. Madsen, S. Ates, T. L. Hansen, A. Löffler, S. Reitzenstein, A. Forchel, and P. Lodahl, "Observation of Non-Markovian dynamics of a single quantum dot in a micropillar cavity," *Phys. Rev. Lett.*, vol. 106, p. 233601, June 2011.

[5] M. Brune, F. S. Kaler, A. Maali, J. Dreyer, E. Hagley, J. M. Raimond, and S. Haroche, "Quantum rabi oscillation: A direct test of field quantization in a cavity," *Phys. Rev. Lett.*, vol. 76, pp. 1800–1803, Mar. 1996.

[6] P. Goy, J. M. Raimond, M. Gross, and S. Haroche, "Observation of Cavity-Enhanced Single-Atom spontaneous emission," *Phys. Rev. Lett.*, vol. 50, pp. 1903–1906, June 1983.

[7] K. Hennessy, A. Badolato, M. Winger, D. Gerace, M. Atature, S. Gulde, S. Falt, E. L. Hu, and A. Imamoglu, "Quantum nature of a strongly-coupled single quantum dot-cavity system," Oct. 2006.

[8] A. Wallraff, D. I. Schuster, A. Blais, L. Frunzio, R. S. Huang, J. Majer, S. Kumar, S. M. Girvin, and R. J. Schoelkopf, "Strong coupling of a single photon to a superconducting qubit using circuit quantum electrodynamics," *NATURE -LONDON-*, vol. 431, pp. 162–166, Sept. 2004.

[9] W. Vogel and D.-G. Welsch, *Quantum Optics.* Wiley-VCH, Aug. 2006.

[10] H. T. Dung, L. Knöll, and D. G. Welsch, "Spontaneous decay in the presence of dispersing and absorbing bodies: General theory and application to a spherical cavity," *Phys. Rev. A*, vol. 62, p. 053804, Oct. 2000.

[11] R. F. Nabiev, P. Yeh, and J. J. S. Mondragon, "Dynamics of the spontaneous emission of an atom into the photon-density-of-states gap: Solvable quantum-electrodynamical model," *Phys. Rev. A*, vol. 47, pp. 3380–3384, Apr. 1993.

[12] I. V. Bondarev, Ya, and S. A. Maksimenko, "Spontaneous decay of excited atomic states near a carbon nanotube," *Phys. Rev. Lett.*, vol. 89, p. 115504, Aug. 2002.

[13] I. V. Bondarev and P. Lambin, "Near-field electrodynamics of atomically doped carbon nanotubes," Jan. 2005.

[14] I. Bondarev, G. Slepyan, and S. Maksimenko, "Photon vacuum renormalization and spontaneous decay of an excited atom near a carbon nanotube," *Optics and Spectroscopy*, vol. 94, pp. 823–828, June 2003.

[15] H. E. Tureci, A. D. Stone, L. Ge, S. Rotter, and R. J. Tandy, "Ab initio self-consistent laser theory and random lasers," *Nonlinearity*, vol. 22, no. 1, pp. C1–C18, 2009.

[16] M. Liertzer, "Nonlinear interactions in coupled microlasers," Master's thesis, Vienna University of Technology, 2011.

[17] H. E. Türeci, A. D. Stone, and B. Collier, "Self-consistent multimode lasing theory for complex or random lasing media," *Phys. Rev. A*, vol. 74, p. 043822, Oct. 2006.

[18] S. Scheel, L. Knöll, and D. G. Welsch, "Spontaneous decay of an excited atom in an absorbing dielectric," *Phys. Rev. A*, vol. 60, pp. 4094–4104, Nov. 1999.

[19] M. Fleischhauer, "Spontaneous emission and level shifts in absorbing disordered dielectrics and dense atomic gases: A green's-function approach," *Phys. Rev. A*, vol. 60, pp. 2534–2539, Sept. 1999.

[20] S. Rotter, "Modular recursive green's function method for quantum transport," Master's thesis, Vienna University of Technology, 1999.

[21] W. H. Press, S. A. Teukolsky, W. T. Vetterling, and B. P. Flannery, *Numerical Recipes 3rd Edition: The Art of Scientific Computing.* Cambridge University Press, 3 ed., Sept. 2007.

[22] J. H. Gordis and B. Neta, "An adaptive method for the numerical solution of volterra integral equations," *Applied and Theoretical Mathematics*, 2000.

[23] O. Svelto, *Principles of Lasers.* Springer, 4 ed., Sept. 2009.